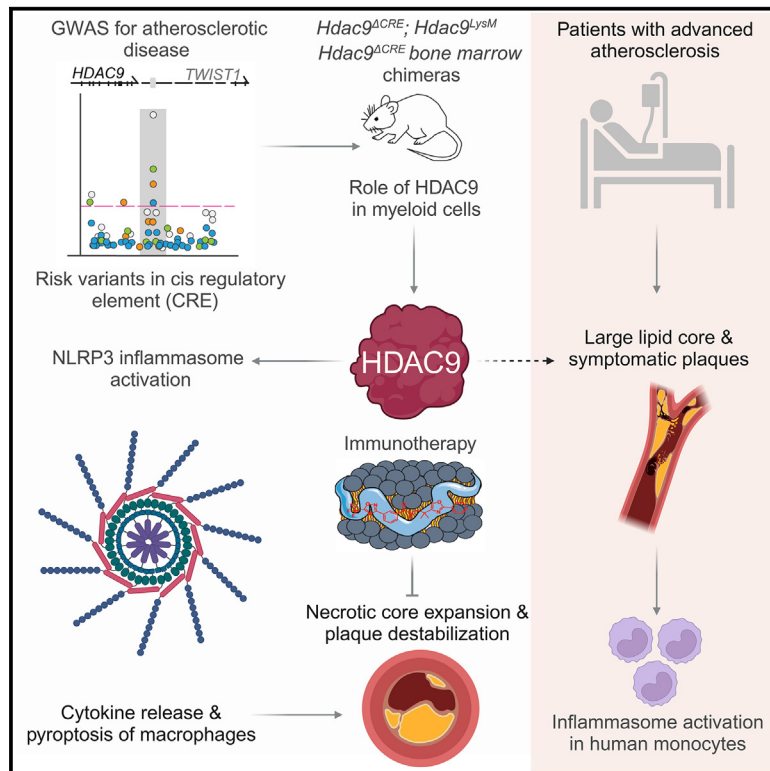


# A *cis*-regulatory element controls expression of histone deacetylase 9 to fine-tune inflammasome-dependent chronic inflammation in atherosclerosis

## Graphical abstract



## Authors

Yaw Asare, Guangyao Yan, Christina Schlegl, ..., Christian Weber, Jürgen Bernhagen, Martin Dichgans

## Correspondence

yaw.asare@med.uni-muenchen.de (Y.A.), martin.dichgans@med.uni-muenchen.de (M.D.)

## In brief

Common genetic variants in a *cis*-regulatory element at *HDAC9*, which regulates expression of the histone deacetylase HDAC9, are a major risk factor for cardiovascular disease. Asare et al. define a mechanism whereby HDAC9 regulates activation of the NLRP3 inflammasome and develop a targeted pharmacological approach that could epitomize a new class of anti-inflammatory therapeutics for atherosclerosis.

## Highlights

- Risk variants in CRE can be leveraged to identify vascular disease mechanisms
- HDAC9 in myeloid cells augments atherosclerotic plaque burden
- HDAC9 is an upstream modulator of NLRP3 inflammasome activation
- Immunotherapy targeting HDAC9 stabilizes atherosclerotic plaques



## Article

# A *cis*-regulatory element controls expression of histone deacetylase 9 to fine-tune inflammasome-dependent chronic inflammation in atherosclerosis

Yaw Asare,<sup>1,13,\*</sup> Guangyao Yan,<sup>1,13</sup> Christina Schlegl,<sup>1</sup> Matthias Prestel,<sup>1</sup> Emiel P.C. van der Vorst,<sup>2,3</sup> Abraham J.P. Teunissen,<sup>4</sup> Arailym Aronova,<sup>1</sup> Federica Tosato,<sup>1</sup> Nawraa Naser,<sup>1</sup> Julio Caputo,<sup>1</sup> Geoffrey Prevot,<sup>4</sup> Anthony Azzun,<sup>4</sup> Benedikt Wefers,<sup>5</sup> Wolfgang Wurst,<sup>5,6</sup> Melanie Schneider,<sup>1</sup> Ignasi Forne,<sup>7</sup> Kiril Bidzhakov,<sup>2</sup> Ronald Naumann,<sup>8</sup> Sander W. van der Laan,<sup>9</sup> Markus Brandhofer,<sup>1</sup> Jiayu Cao,<sup>1</sup> Stefan Roth,<sup>1</sup> Rainer Malik,<sup>1</sup> Steffen Tiedt,<sup>1</sup> Willem J.M. Mulder,<sup>10</sup> Axel Imhof,<sup>7</sup> Arthur Liesz,<sup>1,6</sup> Christian Weber,<sup>2,6,11,12</sup> Jürgen Bernhagen,<sup>1,6,11</sup> and Martin Dichgans<sup>1,5,6,11,14,\*</sup>

<sup>1</sup>Institute for Stroke and Dementia Research (ISD), University Hospital, Ludwig-Maximilian-University (LMU), Munich, Germany

<sup>2</sup>Institute for Cardiovascular Prevention (IPEK), LMU, Munich, Germany

<sup>3</sup>Institute for Molecular Cardiovascular Research (IMCAR), Aachen-Maastricht Institute for CardioRenal Disease (AMICARE) & Interdisciplinary Center for Clinical Research (IZKF), RWTH Aachen University, Aachen, Germany

<sup>4</sup>Biomedical Engineering and Imaging Institute, Icahn School of Medicine at Mount Sinai, New York, NY, USA

<sup>5</sup>Deutsches Zentrum für Neurodegenerative Erkrankungen e. V. (DZNE), Munich, Germany

<sup>6</sup>Munich Cluster for Systems Neurology (SyNergy), Munich, Germany

<sup>7</sup>Protein Analysis Unit, Faculty of Medicine, Biomedical Center, LMU, Martinsried, Germany

<sup>8</sup>Max Planck Institute of Molecular Cell Biology and Genetics, Dresden, Germany

<sup>9</sup>Central Diagnostics Laboratory, Division of Laboratory, Pharmacy, and Biomedical Genetics, University Medical Center Utrecht, University of Utrecht, Utrecht, the Netherlands

<sup>10</sup>Department of Internal Medicine, Radboud Institute of Molecular Life Sciences (RIMLS) and Radboud Center for Infectious Diseases (RCI), Radboud University Nijmegen Medical Center, Laboratory of Chemical Biology, Nijmegen, the Netherlands

<sup>11</sup>German Center for Cardiovascular Research (DZHK), Partner Site Munich Heart Alliance (MHA), Munich, Germany

<sup>12</sup>Department of Biochemistry, Cardiovascular Research Institute Maastricht (CARIM), Maastricht University, Maastricht, the Netherlands

<sup>13</sup>These authors contributed equally

<sup>14</sup>Lead contact

\*Correspondence: yaw.asare@med.uni-muenchen.de (Y.A.), martin.dichgans@med.uni-muenchen.de (M.D.)

<https://doi.org/10.1016/j.immuni.2025.01.003>

## SUMMARY

Common genetic variants in a conserved *cis*-regulatory element (CRE) at histone deacetylase (*HDAC*)9 are a major risk factor for cardiovascular disease, including stroke and coronary artery disease. Given the consistency of this association and its proinflammatory properties, we examined the mechanisms whereby *HDAC*9 regulates vascular inflammation. *HDAC*9 bound and mediated deacetylation of *NLRP3* in the *NACHT* and *LRR* domains leading to inflammasome activation and lytic cell death. Targeted deletion of the critical CRE in mice increased *Hdac9* expression in myeloid cells to exacerbate inflammasome-dependent chronic inflammation. In human carotid endarterectomy samples, increased *HDAC*9 expression was associated with atheroprogession and clinical plaque instability. Incorporation of *TMP195*, a class IIa *HDAC* inhibitor, into lipoprotein-based nanoparticles to target *HDAC*9 at the site of myeloid-driven vascular inflammation stabilized atherosclerotic plaques, implying a lower risk of plaque rupture and cardiovascular events. Our findings link *HDAC*9 to atherogenic inflammation and provide a paradigm for anti-inflammatory therapeutics for atherosclerosis.

## INTRODUCTION

Atherosclerotic cardiovascular disease (CVD), including stroke and myocardial infarction, is the leading cause of death and disability worldwide.<sup>1</sup> Chronic inflammation is a key driver of atheroprogession, whereas resolution of inflammation attenu-

ates disease progression.<sup>2,3</sup> Therefore, extensive efforts are being made to target inflammation in atherosclerotic disease.<sup>2,4</sup> Therapeutic targeting of interleukin (IL)-1 $\beta$  in patients with established atherosclerosis substantially reduces the rate of recurrent cardiovascular events.<sup>5</sup> However, this comes at the cost of increased rates of infection, highlighting the multifaceted effects



of inflammasome-activation-associated cytokines *in vivo*<sup>5,6</sup> and underscoring the need for more targeted anti-inflammatory approaches.

Human genetics is a powerful resource for drug discovery and the prioritization of drug candidates for development.<sup>7–9</sup> Histone deacetylase (*HDAC*)9 is a major risk locus for human atherosclerosis, as revealed by genome-wide association studies (GWASs), in stroke,<sup>7,10</sup> myocardial infarction,<sup>11</sup> and other vascular disorders.<sup>12,13</sup> As with most GWAS loci, the corresponding risk variants are located in non-coding DNA.<sup>14,15</sup> rs2107595, the *HDAC9* lead variant, colocalizes with DNase I-hypersensitive sites and the histone modification marks H3K27ac and H3K4me1. Such marks are frequently found in *cis*-regulatory elements (CREs), which control gene expression in a cell-type-specific manner.<sup>16</sup> Notably, rs2107595 mediates allele-specific transcriptional regulation of *HDAC9*,<sup>17</sup> confirming its effect on gene expression.

*HDAC9* is implicated in the regulation of cell proliferation,<sup>18</sup> pro-inflammatory responses,<sup>19,20</sup> and complex formation with chromatin-modifying enzymes and long non-coding RNA.<sup>21</sup> Of note, *HDAC9* physically interacts with and mediates deacetylation of IKK $\beta$  and TBK1, activating innate immune processes.<sup>19,22</sup> This essential role may partly explain the importance of *HDAC9* as a risk locus for vascular diseases. Here, we examined the mechanisms whereby *HDAC9* promotes vascular inflammation, focusing on the impact of the CRE-driven *HDAC9* expression on atherosclerosis. We exploited information on cell-type-specific mechanisms contained within the CRE by generating a mouse model lacking this element. Through multiple lines of inquiry, we found that *HDAC9* directly interacts with the inflammasome and thereby fine-tunes chronic inflammation in atherosclerosis. In a proof-of-concept therapeutic study, pharmacological inhibition of *HDAC9* in myeloid cells using nanobiologics (NBs) stabilized atherosclerotic plaques, paving the way for a class of immunotherapeutics for the treatment of vascular disease.

## RESULTS

### Targeted deletion of the CRE at the *Hdac9* locus exacerbates atherosclerosis

To study the mechanisms linking genetic risk variants at *HDAC9* to chronic vascular inflammation, we used mouse models of atherosclerosis. The genetic region encompassing rs2107595 is highly conserved across species, with enrichment of active histone marks (Figures 1A and S1A), and targeted deletion of the CRE in human embryonic kidney (HEK) 293 cells resulted in an upregulation of *HDAC9* expression (Figure S1B). We therefore generated mice carrying a deletion of the conserved CRE (1.1 kb; hereafter referred to as *Hdac9* <sup>$\Delta$ CRE</sup>) (Figure 1A), crossed them with *Apoe* <sup>$-/-$</sup>  mice, and examined effects on spontaneous and diet-induced atherosclerosis. *Hdac9* <sup>$\Delta$ CRE</sup>*Apoe* <sup>$-/-$</sup>  mice on a chow diet for 28 weeks developed significantly larger atherosclerotic plaques compared with control *Apoe* <sup>$-/-$</sup>  mice (Figures 1B and 1C), which was associated with an increase in plaque macrophages (M $\phi$ ) (Figures 1D and 1E) and overall increase in pro-inflammatory responses (Figures S1C–S1H). To extend our findings in mice fed a chow diet to conditions of hypercholesterolemia,

we used a model of diet-induced atherosclerosis where *Hdac9* <sup>$\Delta$ CRE</sup>*Apoe* <sup>$-/-$</sup>  and control *Apoe* <sup>$-/-$</sup>  mice received an atherogenic diet for 8 weeks (Figure S1I). Analyses of atherosclerotic plaques revealed an increased plaque burden in *Hdac9* <sup>$\Delta$ CRE</sup>*Apoe* <sup>$-/-$</sup>  mice compared with control *Apoe* <sup>$-/-$</sup>  mice (Figures S1J and S1K), consistent with the model of spontaneous atherosclerosis. Plasma cholesterol levels were unaltered between genotypes (Table S1). Analysis across organs revealed that the CRE controls the expression of *Hdac9* but not *Twist1* (another candidate gene nearby), specifically in the atherosclerotic aorta, without affecting the expression of other *HDACs* (Figures 1F and S2A–S2K). Higher expression of *Hdac9* in the aortas of *Hdac9* <sup>$\Delta$ CRE</sup>*Apoe* <sup>$-/-$</sup>  mice was accompanied by increased plaque inflammation, as demonstrated by enhanced expression of pro-inflammatory cytokines and chemokines, including *Il-1 $\beta$* , *Il-6*, and *Il-18* (Figure 1G). Profiling of 20 circulating cytokines and chemokines in the plasma revealed increased levels of *Il-1 $\beta$* , *Il-6*, and *Il-18* in *Hdac9* <sup>$\Delta$ CRE</sup>*Apoe* <sup>$-/-$</sup>  compared with control *Apoe* <sup>$-/-$</sup>  mice (Figures 1H–1J and S2L–S2T). Thus, the conserved CRE controls *Hdac9* expression to regulate chronic inflammation and atherosclerosis.

### Deletion of the CRE upregulates *Hdac9* expression in myeloid cells to aggravate atherosclerosis

The cell types involved in the pro-atherogenic effects of *Hdac9* remain undefined. Given the known role of CREs in controlling cell-type-specific gene expression and the upregulation of *Hdac9* specifically in atherosclerotic aorta upon deletion of the CRE at *Hdac9*, we examined the effects of this element on *Hdac9* expression in myeloid cells, bone-marrow-derived macrophages (BMDMs), T cells, smooth muscle cells (SMCs), and endothelial cells (ECs) (Figure 2A). Deletion of the CRE increased the expression of *Hdac9* in myeloid cells and BMDMs (Figures 2B and 2C), whereas *HDAC9* expression levels in T cells, SMCs, and ECs remained unaffected in atheroprone and non-hyperlipidemic mice (Figures S3A–S3G). To determine whether CRE-driven expression of *Hdac9* in myeloid cells is sufficient to augment atherosclerotic plaque formation, we performed bone marrow transplantation experiments. Specifically, we reconstituted lethally irradiated recipient *Apoe* <sup>$-/-$</sup>  mice with bone marrow from *Hdac9* <sup>$\Delta$ CRE</sup>*Apoe* <sup>$-/-$</sup>  and control *Hdac9* <sup>$+/+$</sup> *Apoe* <sup>$-/-$</sup>  donors and fed the mice an atherogenic diet for 12 weeks (Figure 2D). Reconstitution with *Hdac9* <sup>$\Delta$ CRE</sup>*Apoe* <sup>$-/-$</sup>  bone marrow exacerbated atherosclerosis (Figures 2E and 2F) and aggravated plaque destabilization (Figures 2G–2I and S3H–S3K). Consistent with these results, *Hdac9* <sup>$\Delta$ CRE</sup>*Apoe* <sup>$-/-$</sup>  BMDMs showed an enhanced pro-inflammatory cytokine expression profile compared with control cells (Figures S3L–S3R). To further scrutinize the effects of *Hdac9* expression in myeloid cells on atherosclerosis, we generated mice with deletion of *Hdac9* in LysM-positive myeloid cells (Figure S4A) and examined the effects on atherosclerotic plaque formation. Myeloid-cell-specific *Hdac9* deletion reduced atherosclerotic plaque size and mitigated plaque destabilization without affecting circulating immune cell counts (Figures 2J–2N and S4B–S4G). Collectively, our results implicate myeloid cells in the pro-atherogenic effects of *Hdac9* and suggest that myeloid-specific deletion of *Hdac9* contributes to atheroprotection and promotes histopathological traits of plaque stability.

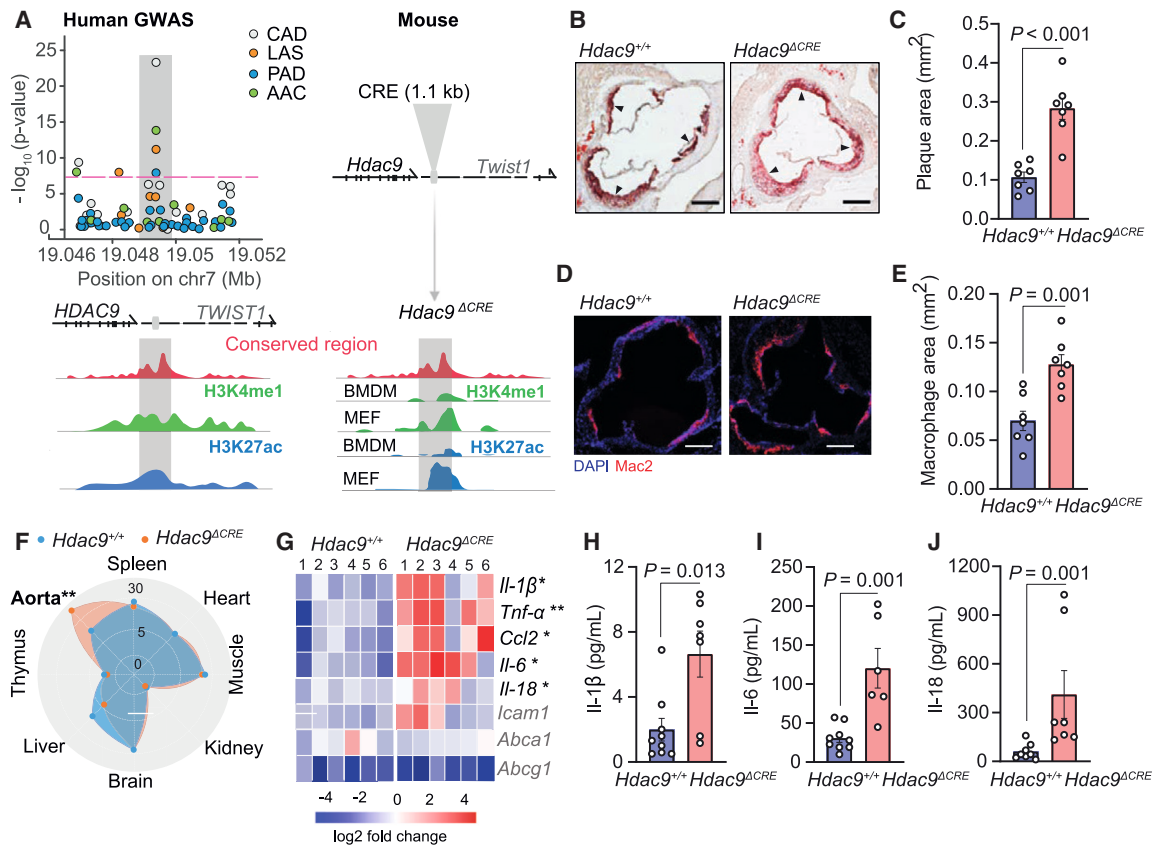


**Figure 1. Targeted deletion of the CRE at *Hdac9* exacerbates atherosclerosis**

(A) Risk variants at *HDAC9* for human atherosclerotic phenotypes are located in the *cis*-regulatory element (CRE), which is conserved across species with enrichment of active histone marks.<sup>23</sup> Shown are all the common variants ±5 kb of the lead signal rs2107595 for coronary artery disease (CAD), large artery stroke (LAS), peripheral artery disease (PAD), and atherosclerotic aortic calcifications (AACs) from the respective GWASs. *Hdac9*<sup>ΔCRE</sup> mice lack 1.1 kb of the CRE. See also Figures S1A and S1B.

(B–E) *Hdac9*<sup>ΔCRE</sup>*Apoe*<sup>-/-</sup> and control *Hdac9*<sup>+/+</sup>*Apoe*<sup>-/-</sup> mice received a chow diet for 28 weeks. (B) Representative oil red O-stained aortic root plaques (indicated by arrowheads). (C) Quantification of aortic root plaque sizes. *n* = 7 mice per genotype. Two-sided unpaired t test. (D) Representative Mac2 immunostaining. (E) Quantification of macrophage area. *n* = 7 mice per genotype. Two-sided unpaired t test. Scale bars, 200 μm in (B) and (D). See also Figures S1C–S1K.

(F and G) *Hdac9*<sup>ΔCRE</sup>*Apoe*<sup>-/-</sup> and control *Hdac9*<sup>+/+</sup>*Apoe*<sup>-/-</sup> mice received a chow diet for 14 weeks. Analysis of the gene expression of *Hdac9* (F) in different tissues normalized to *Hprt1*. *n* = 4–9 mice per genotype. Two-way ANOVA with Sidak’s multiple comparisons test. (G) Measurement of mRNA expression of pro-inflammatory cytokines in atherosclerotic aortas of *Hdac9*<sup>ΔCRE</sup>*Apoe*<sup>-/-</sup> and control *Hdac9*<sup>+/+</sup>*Apoe*<sup>-/-</sup> mice. *n* = 6 mice per group. See also Figures S2A–S2K. (H–J) *Hdac9*<sup>ΔCRE</sup>*Apoe*<sup>-/-</sup> and control *Hdac9*<sup>+/+</sup>*Apoe*<sup>-/-</sup> mice received a chow diet for 28 weeks. Cytokines and chemokines were measured in plasma by the Luminex multiplex cytokine detection platform. *n* = 6–10 mice per genotype. Two-sided Mann-Whitney test (*Il-1β* and *Il-18*) and two-sided unpaired t test (*Il-6*). See also Figures S2L–S2T. Data are mean ± SEM.

### The CRE controls *Hdac9* expression to promote inflammasome activation

The molecular pathways mediating the effects of genetic variation in the *HDAC9* CRE on vascular inflammation and atherosclerosis remain undefined. The observed effects on the circulating levels of *Il-1β*, *Il-6*, and *Il-18* (Figures 1H–1J) pointed toward an effect of *HDAC9* on inflammasome activation. To address this possibility, we stimulated BMDMs from *Hdac9*<sup>ΔCRE</sup>*Apoe*<sup>-/-</sup> and control *Apoe*<sup>-/-</sup> mice with LPS and nigericin and performed bioluminescence assays using the caspase-1 substrate Z-WEHD-aminoluciferin. Compared with control BMDMs, CRE-deleted BMDMs exhibited increased caspase-1 activity (Figure 3A), consistent with increased levels of cleaved caspase-1 (Figures 3B and 3C), indicating enhanced

activation of the inflammasome. Because CREs can regulate distal genes, we performed small interfering RNA (siRNA)-mediated knockdown and overexpression of *Hdac9* in BMDMs and found that the levels of cleaved caspase-1 are indeed altered in an *Hdac9*-dependent manner (Figures S5A–S5E). We therefore hypothesized that *Hdac9* itself is an upstream modulator of inflammasome activation. To test this hypothesis, we used both genetic deletion and pharmacological inhibition of *Hdac9* with the class IIa HDAC inhibitor TMP195, which has high affinity for *HDAC9*<sup>24</sup> and was confirmed to inhibit *HDAC9* in both a cell-free system and in a cell-based (HEK293 cells and *Apoe*<sup>-/-</sup> BMDMs) activity assay (Figures S5F–S5H). We found a reduction in cleaved caspase-1 levels in *Hdac9*-deficient as well as TMP195-treated

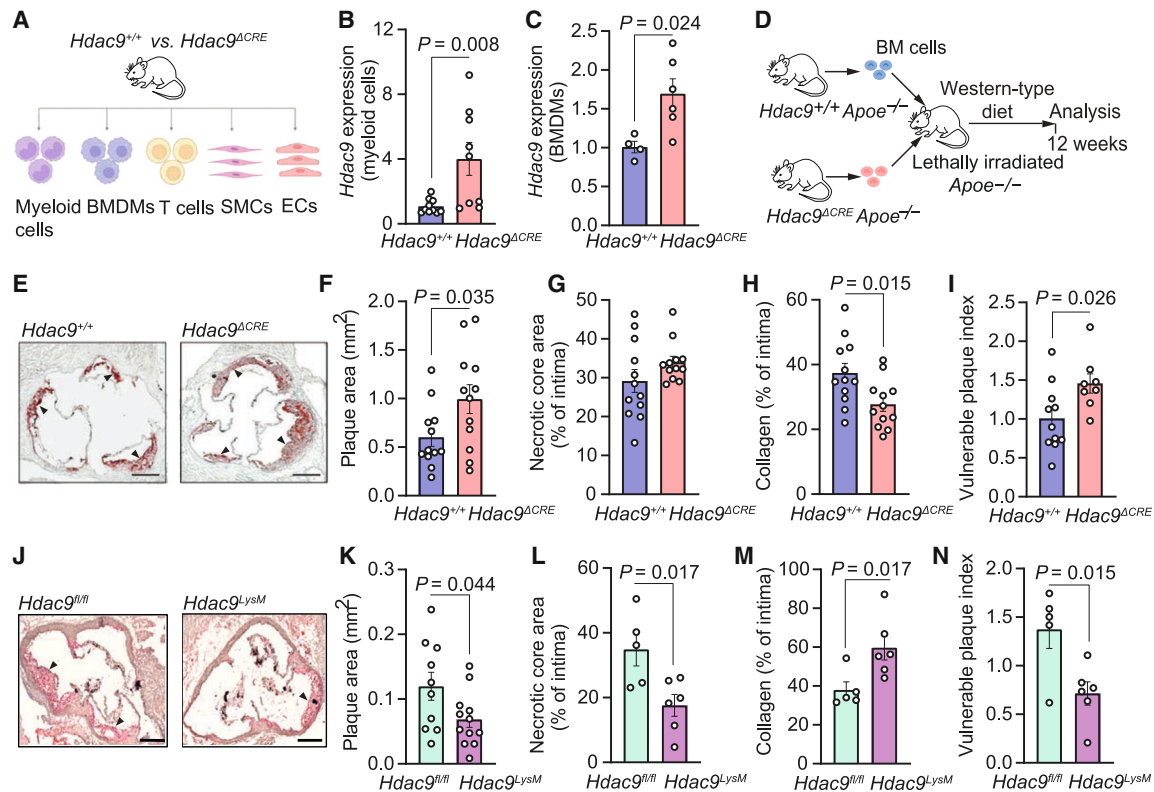


**Figure 2. Deletion of the CRE upregulates *Hdac9* expression in myeloid cells to aggravate atherosclerosis**

(A–C) Analyses of *Hdac9* expression in atherosclerosis-relevant cell types isolated from spleen (myeloid cells), and bone marrow (BMDMs) of *Hdac9*<sup>ΔCRE</sup> *Apoe*<sup>-/-</sup> and control *Hdac9*<sup>+/+</sup> *Apoe*<sup>-/-</sup> mice. (A) Experimental outline. Gene expression of *Hdac9* in CD11b+ myeloid cells (B), and BMDMs (C). T cells, ECs, and SMCs are in Figure S3. *Hprt1* was used as a reference gene.  $n = 4$ –11 mice per genotype. Two-sided unpaired t test. See also Figures S3A–S3G.

(D–I) Lethally irradiated *Apoe*<sup>-/-</sup> mice were reconstituted with bone marrow from either *Hdac9*<sup>ΔCRE</sup> *Apoe*<sup>-/-</sup> (*Hdac9*<sup>ΔCRE</sup>) or *Hdac9*<sup>+/+</sup> *Apoe*<sup>-/-</sup> (*Hdac9*<sup>+/+</sup>) mice and were fed a western-type diet for 12 weeks to induce advanced atherosclerosis. (D) Experimental outline. (E) Representative oil red O-stained aortic root plaques (indicated by arrowheads). (F) Quantification of aortic root plaque sizes.  $n = 12$  mice per genotype. Two-sided unpaired t test. (G) Quantification of necrotic core area. (H) Quantification of collagen content. (I) Overall vulnerability.  $n = 8$ –11 mice per genotype. Two-sided unpaired t test. See also Figures S3H–S3R.

(J–N) Myeloid-specific *Hdac9*-deficient (*Hdac9*<sup>LysM</sup>) and control (*Hdac9*<sup>fl/fl</sup>) mice, all on *Apoe*<sup>-/-</sup> background, received a Western-type diet for 12 weeks. (J) Representative oil red O-stained aortic root plaques (indicated by arrowheads). Scale bars, 200  $\mu$ m. (K) Quantification of aortic root plaque sizes.  $n = 10$ –12 mice per genotype. Two-sided unpaired t test. Advanced plaques were further analyzed. Quantification of necrotic core area (L) and collagen content (M).  $n = 5$ –6 mice per genotype. Two-sided unpaired t test used in (L) and Mann-Whitney test in (M). (N) Vulnerable plaque index.  $n = 5$ –6 mice per genotype. Two-sided unpaired t test. See also Figures S4A–S4G. Data are presented as mean  $\pm$  SEM.

*Apoe*<sup>-/-</sup> BMDMs (Figures 3D and 3E), indicating reduced activation of caspase-1. Upon activation, caspase-1 triggers the maturation and release of IL-1 $\beta$  but also cleaves inactive gasdermin D (GSDMD) to an active pore-forming N-terminal domain GSDMD-N. Accordingly, both *Hdac9*-deficient and TMP195-treated BMDMs released less IL-1 $\beta$  (Figure 3F). We further found a reduction in GSDMD cleavage upon *Hdac9* inhibition (Figures 3G and 3H). This reduced GSDMD-N-dependent pyroptosis in BMDMs, as demonstrated by decreased uptake of the cell death marker Zombie NIR (Figures 3I and S5I) and reduced LDH release (Figure 3J). During physical inflammasome activation, the adaptor protein ASC oligomerizes into a large protein complex and generates a myriad of potential caspase-1 activation sites.<sup>25</sup> Using BMDMs from ASC-citrine reporter mice (ASC<sup>mcitrine</sup>), we analyzed the effect of *Hdac9* inhibition with TMP195 on inflammasome formation by flow cytometry. Inhibition of *Hdac9* reduced inflammasome

activation (Figure S5J) and limited ASC oligomerization (Figure 3K). To corroborate our findings *in vivo*, we examined inflammasome activation in atherosclerotic aortas and plasma from myeloid-cell-specific *Hdac9*-deficient mice receiving an atherogenic diet for 12 weeks. Myeloid-cell-specific deletion of *Hdac9* decreased plaque caspase-1 cleavage (Figures 3L, S5K, and S5L) and reduced circulating levels of IL-1 $\beta$  (Figure 3M), consistent with our *in vitro* findings. To further corroborate the role of NLRP3 inflammasome activation in the pro-atherogenic effect of HDAC9, we treated *Hdac9*<sup>ΔCRE</sup> *Apoe*<sup>-/-</sup> mice receiving an atherogenic diet for 8 weeks with the NLRP3 inhibitor MCC950. The increased atherosclerosis observed in the CRE deleter mice was largely reversed by inactivating the NLRP3 inflammasome with MCC950 (Figures 3N, 3O, S5M, and S5N). Collectively, these findings define inflammasome signaling as a central pathway in CRE-driven vascular inflammation.

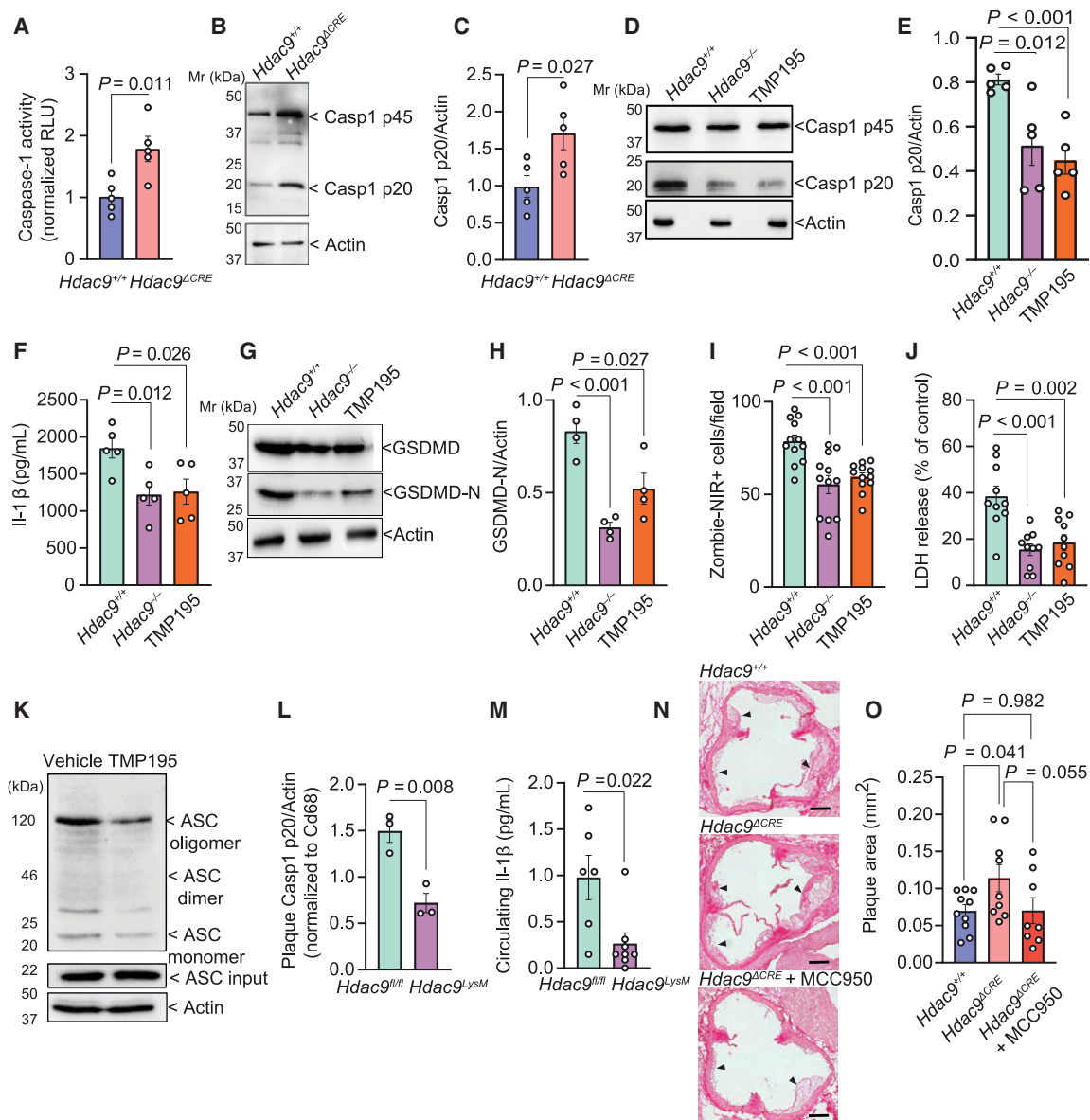


**Figure 3. The CRE controls *Hdac9* expression to promote inflammasome activation**

(A–C) *Hdac9<sup>ΔCRE</sup>Apoe<sup>-/-</sup>* (*Hdac9<sup>ΔCRE</sup>*) and control *Hdac9<sup>+/+</sup>Apoe<sup>-/-</sup>* (*Hdac9<sup>+/+</sup>*) BMDMs were stimulated with LPS (300 ng/mL) for 3 h and nigericin (5  $\mu$ M) for 45 min. (A) Quantification of caspase-1 activity using a bioluminescent Caspase-Glo 1 inflammasome assay kit. RLU indicates relative luciferase units.  $n = 5$  mice per genotype. Two-sided unpaired t test. (B) Representative immunoblot depicting caspase-1 cleavage. Indicated on the left of each membrane is the molecular weight marker in kDa. (C) Quantification of cleaved caspase-1 normalized to actin.  $n = 5$  independent experiments. Two-sided unpaired t test. See also Figures S5A–S5H.

(D–J) Genetic and pharmacological inhibition of Hdac9. *Hdac9<sup>-/-</sup>Apoe<sup>-/-</sup>* (*Hdac9<sup>-/-</sup>*), control *Hdac9<sup>+/+</sup>Apoe<sup>-/-</sup>* (*Hdac9<sup>+/+</sup>*), and TMP195-treated *Apoe<sup>-/-</sup>* BMDMs (TMP195) were stimulated with LPS (100 ng/mL) for 3 h and nigericin (5  $\mu$ M) for 60 min. (D) Representative immunoblot depicting caspase-1 cleavage. (E) Quantification of cleaved caspase-1 normalized to actin.  $n = 5$  independent experiments. Two-sided unpaired t test. (F) Quantification of IL-1 $\beta$  release.  $n = 5$  independent experiments. Two-sided unpaired t test. (G) Representative immunoblot of cleaved GSDMD. (H) Quantification of cleaved GSDMD normalized to actin.  $n = 4$  independent experiments. Two-sided unpaired t test. (I) Quantification of Zombie NIR+ cells.  $n = 4$  independent experiments. Shown is Zombie NIR+ cells/field (3  $\times$  4 fields). Two-sided unpaired t test. See also Figure S5I. (J) Quantification of LDH release. Maximum LDH activity after complete lysis served as a control.  $n = 10$  independent experiments.

(K) Representative immunoblot of ASC oligomerization. Representative of two independent replicates. See also Figure S5J.

(L and M) Myeloid-specific *Hdac9*-deficient (*Hdac9<sup>LysM</sup>*) and control (*Hdac9<sup>fl/fl</sup>*) mice, all on *Apoe<sup>-/-</sup>* background, received a Western-type diet for 12 weeks and the atherosclerotic aortas were isolated and lysed for western blotting. (L) Quantification of cleaved caspase-1 normalized to actin and Cd68.  $n = 3$  mice per genotype. Two-sided unpaired t test. See also Figures S5K and S5L. (M) Quantification of circulating levels of IL-1 $\beta$  (outliers removed after performing ROUT outlier test,  $Q = 1\%$ ). Mann-Whitney test.

(legend continued on next page)

### HDAC9 binds and mediates deacetylation of NLRP3 for inflammasome activation

To understand the underlying molecular mechanism of Hdac9-mediated inflammasome activation, and motivated by the molecular scaffolding function of HDAC9,<sup>26</sup> we hypothesized that HDAC9 is a docking site for cytosolic inflammasome components and facilitates its rapid inflammasome assembly upon stimulation. We performed co-immunoprecipitation experiments and assessed subunits of the inflammasome that would potentially interact with HDAC9. Specifically, we co-transfected V5-HDAC9 and individual components of the inflammasome (FLAG-NLRP3, FLAG-NLRC4, FLAG-AIM2, FLAG-ASC, or FLAG-caspase-1 p45) in pairs into HEK293 cells. We found that HDAC9 specifically interacted with NLRP3 but not with AIM2, NLRC4, ASC, and pro-caspase-1 (p45) (Figures 4A and S5O–S5Q). To substantiate this interaction, we performed co-immunoprecipitation coupled with mass spectrometry as an independent method. Indeed, HDAC9 was one of the interactors of NLRP3 with a high log<sub>2</sub> fold change (>6) (Figure 4B). We next mapped the specific domains of NLRP3 involved in this interaction and found that the ΔPYD, NACHT, LRR, and ΔLRR domains bind to HDAC9, whereas the PYD domain is dispensable for this interaction (Figures 4C and 4D). We further confirmed this binding of HDAC9 to NLRP3 at endogenous levels of both binding partners in human macrophages (Figure 4E). As a last step to corroborate this interaction, we performed micro-scale thermophoresis (MST) analysis by titrating MST-red-NLRP3 against increasing concentrations of HDAC9. The resulting curve indicated a direct interaction between HDAC9 and NLRP3, with a derived *K<sub>D</sub>* value of 733 ± 146 nM (Figure 4F). To scrutinize the molecular consequence and relevance of this interaction, we co-transfected V5-HDAC9 and full-length FLAG-NLRP3 or an NLRP3 mutant lacking the pyrin domain into HEK293 cells and examined the effects on NLRP3 acetylation. Overexpression of HDAC9, mimicking deletion of the CRE (Figure S1B), decreased the acetylation of NLRP3 (Figures 4G and 4H) occurring in the delta PYD domain (NACHT and LRR) of NLRP3 (Figure 4I and S5R). We next assessed the effect of reduced NLRP3 acetylation on the activation step of the inflammasome by analyzing NLRP3 oligomerization and found that HDAC9 promoted the oligomerization of NLRP3 (Figures 4J and 4K). Having demonstrated the role of HDAC9 in inflammasome assembly, we next wished to tease apart its effects on the activation step from the priming. We stimulated BMDMs simultaneously with LPS and nigericin for 60 min, a paradigm that bypasses nuclear factor κB (NF-κB)-dependent transcriptional priming.<sup>27,28</sup> Both, *Hdac9* deletion and treatment with TMP195 reduced rapid caspase-1 activation, as shown by the reduction in the levels of cleaved caspase-1. This also limited the cleavage of inactive GSDMD to the active pore-forming GSDMD-N, thus restricting rapid GSDMD-N-induced pyroptosis of macrophages, as evidenced by reduced LDH release and decreased uptake of Zombie NIR (Figures S6A–S6H). These

findings define the role of HDAC9 in NLRP3 inflammasome assembly without the requirement of NF-κB-driven transcriptional priming, in agreement with the unaltered expression of inflammasome components, including *Nlrp3*, *caspase-1*, *Il-1β*, *ASC*, and *Gsdmd* in *Hdac9*-deficient BMDMs, as shown by RNA sequencing (Figure S6I). Of note, global transcriptional profiling revealed effects of HDAC9 in phases of the cell cycle implicated in unique gene expression programs in macrophages that direct subsequent immunological responses<sup>29</sup> as well as perturbation of gene sets implicated in apoptosis and necrosis (Figures S6J–S6M). This is in line with previous reports implicating HDAC9 in cell-cycle arrest.<sup>17,30</sup> Moreover, the observed dysregulation of programmed cell death and necrosis is in agreement with the pro-inflammatory and pro-atherogenic effects of HDAC9. Hence, our data suggest that HDAC9 may act as a molecular switch in the NLRP3 pathway by controlling the acetylation of NLRP3 specifically in the NACHT and LRR domains for inflammasome activation, a mechanism that could be targeted for vascular protection.

### HDAC9-targeted immunotherapy stabilizes atherosclerotic plaques

Systemic HDAC inhibition by small molecule drugs is associated with side effects including cardiotoxicity.<sup>31</sup> Targeting therapeutics to relevant tissues or cell populations can limit potential systemic side effects while increasing efficacy.<sup>32,33</sup> Having demonstrated that the CRE drives *HDAC9* expression to fine-tune inflammasome activation specifically in myeloid cells, we aimed to pharmacologically inhibit Hdac9 in this cell population. To achieve this, we incorporated TMP195 into lipoprotein-based nanoparticles, named NBs.<sup>34</sup> We examined the effects of TMP195 NBs (TMP195-NB) on established atherosclerosis. 8-week-old *Apoe*<sup>-/-</sup> mice receiving an atherogenic diet for 8 weeks were treated with TMP195-NB or unloaded NBs (placebo) starting from the fifth week of diet, when plaques had developed (Figure 5A). The overall dose of TMP195-NB (10 mg/kg twice a week for 4 weeks) was about 17-fold lower than in our previous study in which TMP195 was administered systemically with daily injections for 4 weeks.<sup>19</sup> Circulating myeloid cell counts remained unchanged in treated animals (Figures S7A–S7D). Yet, TMP195-NB treatment showed beneficial effects on atherosclerotic plaque stability, with a trend toward reduction in plaque size, a significant reduction in necrotic core area, and increased deposition of collagen in atherosclerotic plaques, resulting in increased plaque stability (Figures 5B–5D and S7E–S7L). Hence, therapeutic inhibition of HDAC9 in myeloid cells may provide a strategy for the treatment of atherosclerotic vascular inflammation. To further evaluate the translational potential of our findings, we analyzed carotid atherosclerotic plaque specimens from patients who had undergone endarterectomy for the treatment of symptomatic or asymptomatic carotid stenosis (Figure 5E) and examined the association between *HDAC9* expression and histopathological

(N and O) *Hdac9*<sup>ΔCRE</sup>*Apoe*<sup>-/-</sup> mice receiving Western-type diet for 8 weeks were treated with the NLRP3 inhibitor MCC950 (10 mg/kg) three times a week in parallel to the diet feeding. Control *Hdac9*<sup>+/+</sup>*Apoe*<sup>-/-</sup> and *Hdac9*<sup>ΔCRE</sup>*Apoe*<sup>-/-</sup> mice were also placed on a Western-type diet for 8 weeks and received PBS as vehicle control. (N) Representative Picro-Sirius red-stained aortic root plaques (indicated by arrowheads). Scale bars = 200 μm. (O) Quantification of plaque sizes. One-way ANOVA with two-stage setup method of Benjamini, Krieger, and Yekutieli multiple comparisons test. See also Figures S5M and S5N. Data are mean ± SEM.

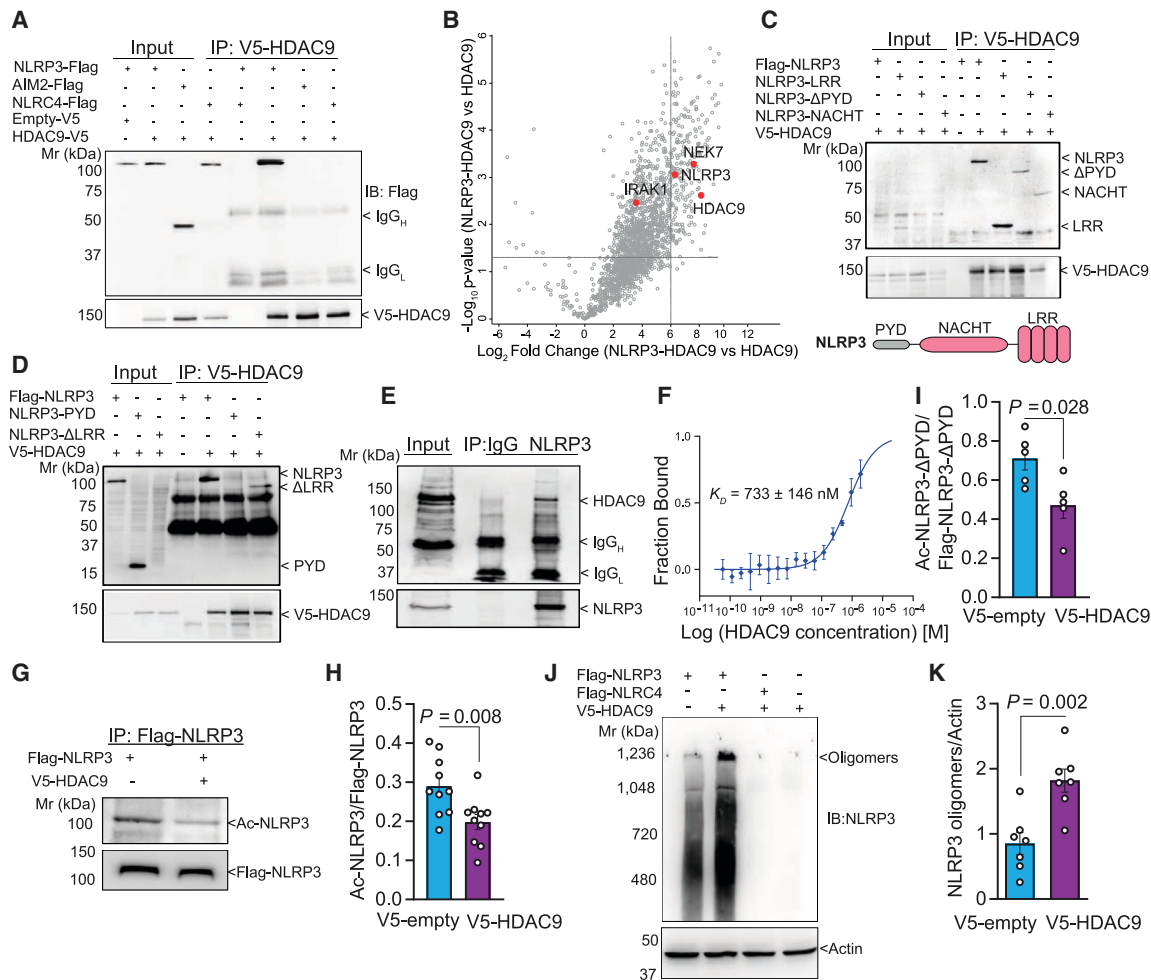


**Figure 4. HDAC9 binds and mediates deacetylation of NLRP3 for inflammasome activation**

(A) HEK293 cells were transiently co-transfected with V5-HDAC9 or V5-empty control vector and FLAG-tagged full-length NLRP3, NLRP3, or AIM2. Shown are representative immunoblots depicting the binding of HDAC9 to NLRP3, but not NLRP3, and AIM2.  $n = 4$  independent experiments. See also Figures S50–S5Q. (B) HEK293 cells were transiently co-transfected with V5-HDAC9 and FLAG-tagged full-length NLRP3. Liquid chromatography–tandem mass spectrometry (LC–MS/MS) analysis showing interactors of NLRP3.  $n = 4$  independent experiments. (C and D) Representative immunoblots depicting the binding of HDAC9 to specific domains of NLRP3 (all FLAG-tagged).  $n = 3–4$  independent experiments. Shown below (C) is a cartoon depicting NLRP3 domains. (E) THP1 macrophages were challenged with LPS (200 ng/mL) for 6 h, followed by stimulation with 5  $\mu$ M of nigericin for 60 min. Endogenous NLRP3 (bottom) was immunoprecipitated with an anti-NLRP3 antibody and endogenous HDAC9 (upper) was revealed by an anti-HDAC9 antibody. Shown are representative immunoblots depicting the binding of HDAC9 to NLRP3 at endogenous level.  $n = 3$  independent experiments. Bands for HDAC9 and NLRP3 as well as IgG<sub>H</sub> and IgG<sub>L</sub> (as immunoprecipitation [IP] side products) are indicated. (F) Protein–protein interactions between HDAC9 and NLRP3 were analyzed in solution applying MST. 15 nM MST-red-NLRP3 was titrated against increasing concentrations of HDAC9. Plotted is the fraction of bound MST-red-NLRP3 (fraction bound) over the indicated concentrations of HDAC9 (log scale). Data are mean  $\pm$  SD, with 4 data points for each concentration of HDAC9. Two independent titrations measured in two separate sets of capillaries. (G–K) HEK293 cells were transiently co-transfected with V5-HDAC9 and FLAG-tagged full-length or mutant NLRP3. (G) Representative immunoblot of acetylation of NLRP3. (H) Quantification of acetylated NLRP3 normalized to actin.  $n = 10$  independent experiments. Two-sided unpaired t test. (I) Quantification of acetylated NLRP3- $\Delta$ PYD normalized to actin. Representative immunoblots are shown in Figure S5R.  $n = 5$  independent experiments. Two-sided unpaired t test. See also Figure S5R. (J) Representative immunoblot showing NLRP3 oligomerization in transfected HEK293 cells stimulated with nigericin and analyzed by blue native PAGE. (K) Quantification of NLRP3 oligomers normalized to actin.  $n = 7$  independent experiments. Two-sided unpaired t test. Data are mean  $\pm$  SEM.

features of plaque instability, including lipid core, VSMC burden, and macrophage content. *HDAC9* expression in human atherosclerosis was associated with a large lipid core (>10%) and lower VSMC burden (no/minor), with no effect on macrophage content in models adjusting for age, sex, and vascular risk factors (Figures 5F and S8A–S8C). Integrating all features of plaque

instability, higher expression of *HDAC9* was associated with increased plaque instability in humans (Figure 5G), underscoring the clinical relevance of our experimental findings in mice. We further explored associations between plaque *HDAC9* expression and clinical plaque instability. *HDAC9* expression in the plaque was higher among individuals with symptomatic plaque (that

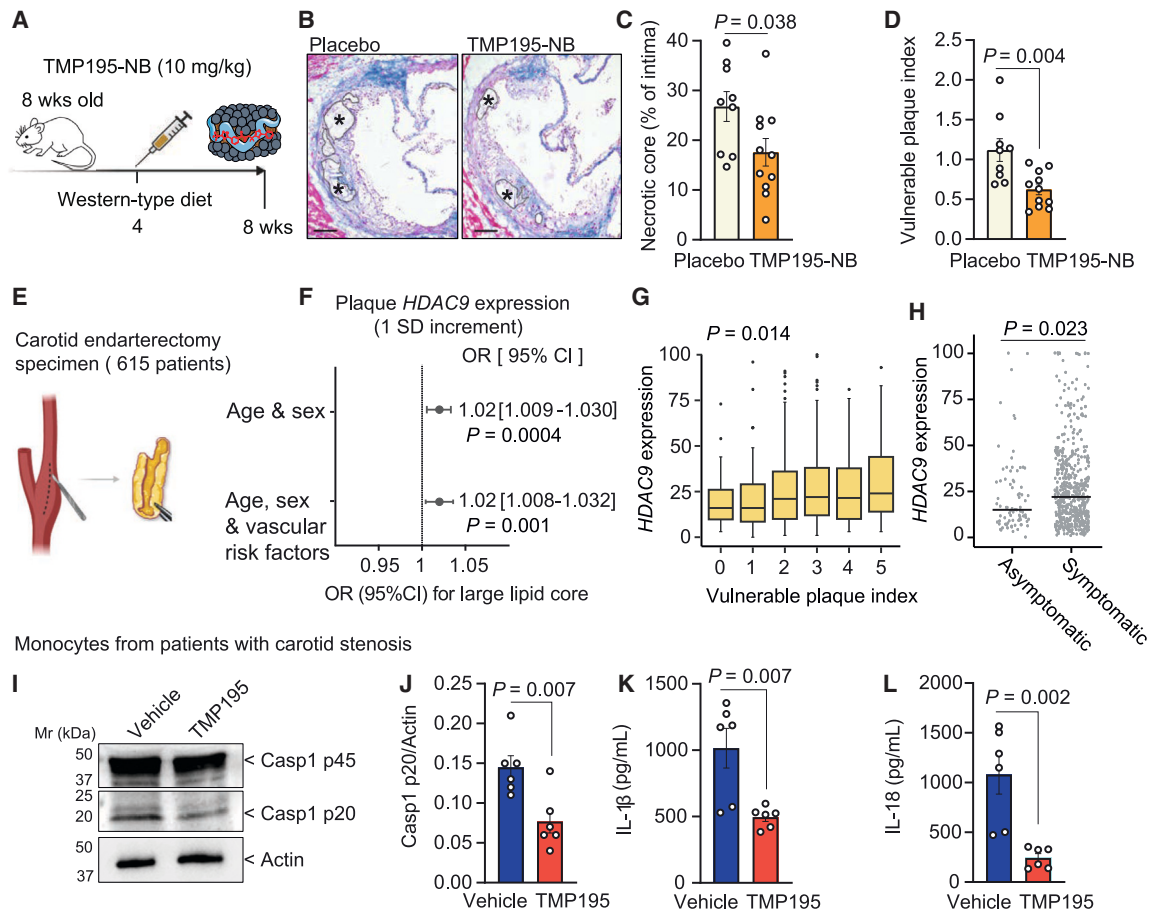


**Figure 5. HDAC9-targeted immunotherapy stabilizes atherosclerotic plaques**

(A–D) *Apoe*<sup>−/−</sup> mice receiving Western-type diet for 8 weeks were treated with TMP195-NB (10 mg/kg) or placebo twice a week starting from the 5<sup>th</sup> week of diet, when plaques have already developed. (A) Experimental outline. (B) Representative Masson trichrome staining. Dashed lines and asterisks indicate necrotic core areas. (C) Quantification of necrotic core area. *n* = 9–11 mice per genotype. Two-sided unpaired t test. (D) Vulnerable plaque index. *n* = 9–11 mice per genotype. Two-sided unpaired t test. See also [Figures S7A–S7L](#).

(E–H) Carotid atherosclerotic plaque specimens from patients who underwent endarterectomy for treatment of symptomatic or asymptomatic carotid stenosis were analyzed. (E) Experimental outline. (F) Associations of plaque *HDAC9* expression (1 SD increment) with large lipid core (binary traits) as derived from logistic regression analyses adjusted for age, sex, and vascular risk. Shown are odds ratios (ORs) and the 95% confidence interval. *N* = 615 individuals (age and sex adjusted) and *N* = 530 individuals (age, sex, and vascular risk factors adjusted). See also [Figures S8A–S8C](#). (G) Plaque *HDAC9* expression (inverse-rank transformed) in study participants across vulnerable plaque index scores (*p* value derived from Kruskal-Wallis test). Shown are the median values (central line), the upper and lower quartiles (box limits) and the 1.5 × interquartile range (whiskers). 12 outlier observations with *HDAC9* expression levels > 100 are not displayed for graphical reasons. Statistics reported with raw data; associations without outliers show a *p* value = 0.023. (H) Plaque *HDAC9* expression (inverse-rank transformed) in patients with symptomatic vs. asymptomatic plaques (*p* value derived from Mann-Whitney U test).

(I–L) Monocytes were freshly isolated from patients with advanced atherosclerosis (*n* = 6) and treated *ex vivo* with TMP195 or vehicle for 1 h prior to stimulation with LPS (100 ng/mL) for 3 h and nigericin (5 μM) for 60 min. (I) Representative immunoblot of caspase-1 cleavage. (J) Quantification of cleaved caspase-1 normalized to actin. *n* = 6 independent experiments. Two-sided unpaired t test. Quantification of IL-1β (K) and IL-18 (L) release. *n* = 6 independent experiments. Two-sided unpaired t test. See also [Figures S8D](#) and [S8E](#). Data are mean ± SEM.

had caused an acute cerebrovascular event) compared with individuals with asymptomatic plaques ([Figure 5H](#)). To further test the translational relevance of our findings, we assessed whether the association between *HDAC9* expression and large lipid core in human atherosclerosis may involve alterations in NLRP3 inflammasome signaling. For this, we isolated monocytes from patients with advanced carotid atherosclerosis ([Table S2](#)) and treated them *ex vivo* with TMP195 for 1 h before priming with LPS for 3 h and activation of the inflammasome with nigericin for 1 h. Pharmacological inhibition with TMP195 limited inflam-

masome activation, as demonstrated by reduced caspase-1 cleavage and the release of IL-1β and IL-18 ([Figures 5I–5L](#)). To distinguish NF-κB-dependent transcriptional priming and the activation step of the NLRP3 inflammasome, we again isolated monocytes from patients with advanced carotid atherosclerosis and treated them *ex vivo* with TMP195 for 1 h before co-stimulation with LPS and nigericin for 1 h. We found that TMP195 treatment reduced the cleavage of caspase-1 and, hence, inflammasome activation, without the requirement for NF-κB-driven transcriptional priming ([Figures S8D](#) and [S8E](#)). Collectively,

these results show that HDAC9-targeted therapy reduces necrotic core expansion to mitigate atherosclerotic plaque destabilization, consistent with a significant association of *HDAC9* expression with large lipid cores and plaque instability in human atherosclerosis.

## DISCUSSION

Despite the success of lipid-lowering therapy and additional measures to mitigate the complications of atherosclerosis, CVD remains the leading cause of death worldwide. The importance of immune mechanisms in atherosclerosis is undisputed.<sup>2,4,35</sup> Indeed, the CANTOS, COLCOT, and LoDoCo2 trials provided proof-of-concept evidence that targeting chronic inflammation can lower CVD risk,<sup>5,36,37</sup> thus setting the stage for a new paradigm of anti-inflammatory and atheroprotective treatments.

Our current results suggest that therapeutic inhibition of HDAC9, a target supported by human genetics, may provide an effective lever for fine-tuning inflammasome-dependent chronic inflammation in atherosclerosis. We showed that (1) deletion of the conserved non-coding CRE 3' at *HDAC9* upregulated *Hdac9* expression in myeloid cells to exacerbate atherosclerosis, (2) *Hdac9* bound to and mediated deacetylation of NLRP3 to unleash inflammasome activation and pyroptotic cell death, and (3) genetic and pharmacological inhibition of *Hdac9* in myeloid cells stabilized atherosclerotic plaques by reducing necrotic core expansion. The association between increased *HDAC9* expression in human atherosclerotic plaques with large lipid cores and alterations of NLRP3 inflammasome activation in isolated monocytes further substantiated the translational potential of HDAC9 as a druggable regulator of inflammasome activity.

Therapeutic inhibition of HDAC9 may present advantages over blockade of IL-1 $\beta$ . First, HDAC9 bound specifically to NLRP3 but not the other inflammasome sensors, such as AIM2 and NLRC4, which are also involved in IL-1 $\beta$  production and recognition of pathogens. Hence, targeted inhibition of HDAC9 can be expected to have no substantial effects on anti-microbial capacities of the immune response to infections. Second, inhibition of HDAC9 reduced IL-18 and pyroptotic cell death, which would provide additional atheroprotection. Third, HDAC9 is pro-atherogenic in both early and advanced atherosclerosis in contrast to IL-1 $\beta$ , which shows atheroprotective effects in advanced atherosclerosis.<sup>38</sup> Hence, pharmacological inhibition of HDAC9 might provide a more specific and less harmful therapeutic strategy for vascular protection.

Approximately 90% of GWAS signals reside in non-coding sequences, particularly CRE,<sup>39</sup> which are required for temporal and spatial control of gene expression and thus could explain their involvement in human disease.<sup>15,40</sup> Previous studies attempted to link human genetic variation in CRE to vascular inflammation,<sup>41–43</sup> but, to our knowledge, none of them demonstrated causality in animal models of chronic vascular disease. The *Hdac9* <sup>$\Delta$ CRE</sup> mice introduced here provide compartment-specific information on the regulatory function of the CRE while maintaining the transcriptional fidelity during atherogenesis. Our data indicating a myeloid-specific regulatory role of the conserved CRE in mice is consistent with previous reports showing that

rs2107595 upregulates *HDAC9* expression in human PBMCs but not in vascular cells.<sup>17</sup> This might relate to cell-type-specific chromatin conformation affecting the accessibility of transcription factors and thus gene expression.<sup>44,45</sup> The effects of CRE-driven *Hdac9* expression on innate immune mechanisms, including inflammasome-dependent cytokine production and caspase-1 activation, further highlight the potential of exploiting information from CRE in identifying relevant cell types and mechanisms by which genetic variants influence disease.

Untargeted inhibition of inflammasome-mediated cytokines may have adverse effects. The increased infection rate observed with therapeutic inhibition of IL-1 $\beta$ <sup>5</sup> underscores the need to better understand the molecular mechanisms of inflammasome activation and to identify alternative therapeutic targets and strategies for atheroprotection. The previously unrecognized activating effect of HDAC9 on the NLRP3-inflammasome-driven signaling cascade unraveled here provides a strategy to fine-tune inflammasome-dependent immune responses to reduce atherosclerotic CVD. This involves HDAC9-mediated deacetylation of NLRP3 and subsequent activation of the inflammasome. The effects of acetylation on inflammasome activation appear to be dependent on the sensor and the specific domains involved. Although SIRT2-mediated deacetylation of NLRP3 in the pyrin domain inhibits inflammasome activation, deacetylation of NLRC4 by SIRT3 in the CARD and nucleotide-binding domain promotes the activation of the inflammasome.<sup>46,47</sup> Our finding that HDAC9 bound to and mediated deacetylation of NLRP3 in the NACHT and LRR domains to promote inflammasome activation supports the notion that domain-specific acetylation of NLRP3 leads to differential effects on inflammasome activation. Such differential effects on inflammasome activation by post-translational modification have been described for phosphorylation of NLRP3.<sup>48</sup> Inflammasome activation involves caspase-1-dependent cleavage of GSDMD, allowing GSDMD-N to form pores in the plasma membrane and facilitating the release of matured IL-1 $\beta$  and IL-18. Pore-forming GSDMD-N further induces pyroptosis, an inflammatory form of cell death.<sup>49</sup> Our finding that HDAC9 modulated inflammasome-mediated GSDMD activation and pyroptotic cell death fits with the reduced necrotic core expansion and plaque destabilization demonstrated here in experimental paradigms of HDAC9 inactivation and immunotherapeutic inhibition. Nonetheless, we cannot fully exclude the involvement of other HDAC9-mediated mechanisms, including effects on epigenetic regulation and the activation of IKK. Moreover, IKK is required for inflammasome formation independent of transcriptional priming.<sup>27,28</sup> Hence, we believe that the dual effects of HDAC9 on IKK activity<sup>19</sup> and NLRP3 acetylation synergize to enhance inflammasome formation, resulting in increased caspase-1 activation, IL-1 $\beta$  maturation, and GSDMD-mediated pyroptosis, mechanisms that promote pro-inflammatory responses in the vessel wall.

Contraindications to the application of broad-spectrum HDAC inhibitors have limited their use in CVD.<sup>50</sup> For example, treatment with trichostatin A exacerbates atherosclerotic plaque formation<sup>51</sup> despite inhibitory effects on macrophage function.<sup>52</sup> The strategy presented here may help in overcoming this limitation by restricting the inhibitory effects to individual HDACs and specifically targeting myeloid cells. Cell-type-specific targeting strategies have shown promise in reducing adverse effects while

enhancing efficacy.<sup>32,33</sup> Thus, our current findings in mice with myeloid-specific deletion of *Hdac9* and with NBs specifically delivering Hdac9 inhibitor to myeloid cells provide a blueprint for future precision medicine approaches targeting individual HDACs and specific cell populations without interfering with the potential protective effects of HDAC9.<sup>53</sup> This can be extended to other conditions, given the central role of chronic inflammation in the pathogenesis of a wide range of diseases and the need for targeted anti-inflammatory therapies.<sup>49</sup>

### Limitations of the study

The phenotype of human atherosclerotic plaques, including instability, plaque rupture, and erosion with occlusive thrombosis, is not fully mimicked by animal models of atherosclerosis. Therefore, despite the confirmation of a link between increased *HDAC9* expression and both atheroprotection, clinical plaque instability, and altered inflammasome activation in monocytes from patients with advanced atherosclerosis, further studies are needed to determine whether the mechanisms described here also apply to atheroprotection in humans. In addition, the HDAC9 immunotherapy approach described in the current work represents a paradigm for future studies and will further benefit from testing its efficacy in humanized models of atherosclerosis. The development of small molecule inhibitors with even higher specificity for HDAC9 may also be helpful in realizing the full potential of HDAC9 inhibition for the prevention of atherosclerosis.

### RESOURCE AVAILABILITY

#### Lead contact

Further information and requests for resources and reagents should be directed to and will be fulfilled by the lead contact, Martin Dichgans ([martin.dichgans@med.uni-muenchen.de](mailto:martin.dichgans@med.uni-muenchen.de)).

#### Materials availability

Reagents generated in this study are available from the [lead contact](#) with a completed Material Transfer Agreement.

#### Data and code availability

The mass spectrometry proteomics data have been deposited to the ProteomeXchange Consortium via the PRIDE partner repository with the dataset identifier PRIDE: PXD042078. Transcriptomics data are available online under the accession number GEO: GSE274312. The data used for the association studies in human carotid atherosclerosis are available through DataverseNL and the codes used are available through a GitHub repository. Data: Athero-Express clinical data, <https://doi.org/10.34894/4IKE3T>; histological data, <https://doi.org/10.34894/Q1135J>; bulk transcriptomics data, <https://doi.org/10.34894/D1MDKL>. Code: [https://github.com/CirculatoryHealth/AE\\_20211201\\_YAW\\_SWWANDERLAAN\\_HDAC9](https://github.com/CirculatoryHealth/AE_20211201_YAW_SWWANDERLAAN_HDAC9). All other relevant data are in the manuscript and available from the [lead contact](#) on reasonable request.

### ACKNOWLEDGMENTS

We are grateful to Drs. Veit Hornung, Florian Schmidt, and Peter Düwell for advice and sharing of constructs. We thank Dr. Marios Georgakis for discussions on the recruitment of human subjects and analysis of carotid atherosclerosis plaque samples from Athero-Express Biobank. We also thank Barbara Lindner and Alessia Nottebrock for technical assistance.

This work was supported by grants from the Deutsche Forschungsgemeinschaft (DFG; CRC 1123 [B3], DI-722/16-1 [ID: 428668490], DI 722/21-1, and Munich Cluster for Systems Neurology [SyNergy, EXC 2145]), the Vascular Dementia Research Foundation, and the European Union's Horizon Europe (European Innovation Council) programme under grant agreement no. 101115381

to M.D. Y.A. was supported by DFG (CRC 1123 [B3], AS 575/1-1) and Fritz Thyssen Foundation (10.24.2.001MN). J.B. received funding from DFG/CRC 1123 (A3), DFG INST 409/209-1 FUGG, DFG (EXC 2145 SyNergy), and the m<sup>4</sup> award program of the Bavarian Ministry of Economic Affairs. C.W. was supported by DFG (CRC 1123 [A01 & A10]), by the European Research Council (ERC AdG 692511), and by the DZHK (German Centre for Cardiovascular Research) and the BMBF (German Ministry of Education and Research). A.I. was supported by DFG (CRC 1123 [Z02]) and the Bundesministerium für Bildung und Forschung (BMBF; FKZ161L0214F). E.P.C.v.d.V. is supported by the Interdisciplinary Center for Clinical Research at the RWTH Aachen University, DFG (SFB TRR219-M07) and the Corona Foundation (S199/10084/2021).

### AUTHOR CONTRIBUTIONS

Y.A. and M.D. conceived and designed the experiments with input from M.P. Y.A., G.Y., and C.S. performed most experiments and analyzed data; M.P., E.P.C.v.d.V., A.J.P.T., A. Aronova, F.T., N.N., J. Caputo, G.P., A. Azzun, M.S., I.F., M.B., J. Cao, S.R., and A.I. performed experiments and analyzed data; S.W.v.d.L. provided and analyzed data from human carotid endarterectomy; B.W., W.W., K.B., R.N., R.M., S.T., W.J.M.M., A.L., C.W., and J.B. contributed critical material and techniques for this study; A.L. and J.B. contributed critical input to study design and manuscript writing. Y.A. and M.D. wrote the manuscript with input from all authors.

### DECLARATION OF INTERESTS

The authors declare no competing interests.

### STAR★METHODS

Detailed methods are provided in the online version of this paper and include the following:

- **KEY RESOURCES TABLE**
- **EXPERIMENTAL MODEL AND STUDY PARTICIPANT DETAILS**
  - Human atherosclerosis study subjects
  - Histopathologic analysis of human atherosclerotic plaque composition
  - Blood sampling from patients with atherosclerosis
  - Generation of mice lacking the CRE at *Hdac9* (*Hdac9<sup>ΔCRE</sup>*)
  - Conditional inactivation of *Hdac9* gene in mice
- **METHOD DETAILS**
  - Isolation of human monocytes
  - Mouse model of atherosclerosis
  - Bone Marrow Transplantation
  - Formulating and characterizing TMP195-loaded nanobiologics
  - Treatment of atherosclerosis with the inhibitor MCC950 or TMP195-nanobiologics
  - Immunohistochemistry
  - Cell lysis, co-immunoprecipitation and Western blot analysis
  - LC-MS/MS analysis
  - Microscale thermophoresis (MST) measurements
  - Confocal Microscopy
  - Multiplex cytokine profiling assay
  - Cell culture, transfection, and gene silencing
  - Generation of bone marrow-derived macrophages
  - Inflammasome activation assay
  - Blue native gel electrophoresis for NLRP3 oligomerization
  - ASC oligomerization
  - HDAC9 activity assay
  - ELISA
  - Detection of lytic cell death
  - Flow cytometry
  - Transcriptomic profiling
  - Quantitative real-time PCR
  - Magnetic activated cell sorting (MACS)
  - Statistical tests

## SUPPLEMENTAL INFORMATION

Supplemental information can be found online at <https://doi.org/10.1016/j.immuni.2025.01.003>.

Received: January 24, 2024  
Revised: September 3, 2024  
Accepted: January 3, 2025  
Published: January 28, 2025

## REFERENCES

- Mensah, G.A., Roth, G.A., and Fuster, V. (2019). The Global Burden of Cardiovascular Diseases and Risk Factors: 2020 and Beyond. *J. Am. Coll. Cardiol.* *74*, 2529–2532. <https://doi.org/10.1016/j.jacc.2019.10.009>.
- Soehnlein, O., and Libby, P. (2021). Targeting inflammation in atherosclerosis - from experimental insights to the clinic. *Nat. Rev. Drug Discov.* *20*, 589–610. <https://doi.org/10.1038/s41573-021-00198-1>.
- Roy, P., Orecchioni, M., and Ley, K. (2022). How the immune system shapes atherosclerosis: roles of innate and adaptive immunity. *Nat. Rev. Immunol.* *22*, 251–265. <https://doi.org/10.1038/s41577-021-00584-1>.
- Engelen, S.E., Robinson, A.J.B., Zurke, Y.X., and Monaco, C. (2022). Therapeutic strategies targeting inflammation and immunity in atherosclerosis: how to proceed? *Nat. Rev. Cardiol.* *19*, 522–542. <https://doi.org/10.1038/s41569-021-00668-4>.
- Ridker, P.M., Everett, B.M., Thuren, T., MacFadyen, J.G., Chang, W.H., Ballantyne, C., Fonseca, F., Nicolau, J., Koenig, W., Anker, S.D., et al. (2017). Antiinflammatory Therapy with Canakinumab for Atherosclerotic Disease. *N. Engl. J. Med.* *377*, 1119–1131. <https://doi.org/10.1056/NEJMoa1707914>.
- Sharma, B.R., and Kanneganti, T.D. (2021). NLRP3 inflammasome in cancer and metabolic diseases. *Nat. Immunol.* *22*, 550–559. <https://doi.org/10.1038/s41590-021-00886-5>.
- Mishra, A., Malik, R., Hachiya, T., Jürgenson, T., Namba, S., Posner, D.C., Kamanu, F.K., Koido, M., Le Grand, Q., Shi, M., et al. (2022). Stroke genetics informs drug discovery and risk prediction across ancestries. *Nature* *611*, 115–123. <https://doi.org/10.1038/s41586-022-05165-3>.
- Nelson, M.R., Tipney, H., Painter, J.L., Shen, J., Nicoletti, P., Shen, Y., Floratos, A., Sham, P.C., Li, M.J., Wang, J., et al. (2015). The support of human genetic evidence for approved drug indications. *Nat. Genet.* *47*, 856–860. <https://doi.org/10.1038/ng.3314>.
- Plenge, R.M., Scolnick, E.M., and Altshuler, D. (2013). Validating therapeutic targets through human genetics. *Nat. Rev. Drug Discov.* *12*, 581–594. <https://doi.org/10.1038/nrd4051>.
- Malik, R., Chauhan, G., Traylor, M., Sargurupremraj, M., Okada, Y., Mishra, A., Ruten-Jacobs, L., Giese, A.K., van der Laan, S.W., Gretarsdottir, S., et al. (2018). Multiancestry genome-wide association study of 520,000 subjects identifies 32 loci associated with stroke and stroke subtypes. *Nat. Genet.* *50*, 524–537. <https://doi.org/10.1038/s41588-018-0058-3>.
- Aragam, K.G., Jiang, T., Goel, A., Kanoni, S., Wolford, B.N., Atri, D.S., Weeks, E.M., Wang, M., Hindy, G., Zhou, W., et al. (2022). Discovery and systematic characterization of risk variants and genes for coronary artery disease in over a million participants. *Nat. Genet.* *54*, 1803–1815. <https://doi.org/10.1038/s41588-022-01233-6>.
- Klarin, D., Lynch, J., Aragam, K., Chaffin, M., Assimes, T.L., Huang, J., Lee, K.M., Shao, Q., Huffman, J.E., Natarajan, P., et al. (2019). Genome-wide association study of peripheral artery disease in the Million Veteran Program. *Nat. Med.* *25*, 1274–1279. <https://doi.org/10.1038/s41591-019-0492-5>.
- Malhotra, R., Mauer, A.C., Lino Cardenas, C.L., Guo, X., Yao, J., Zhang, X., Wunderer, F., Smith, A.V., Wong, Q., Pechlivanis, S., et al. (2019). HDAC9 is implicated in atherosclerotic aortic calcification and affects vascular smooth muscle cell phenotype. *Nat. Genet.* *51*, 1580–1587. <https://doi.org/10.1038/s41588-019-0514-8>.
- Watanabe, K., Stringer, S., Frei, O., Umičević Mirkov, M., de Leeuw, C., Polderman, T.J.C., van der Sluis, S., Andreassen, O.A., Neale, B.M., and Posthuma, D. (2019). A global overview of pleiotropy and genetic architecture in complex traits. *Nat. Genet.* *51*, 1339–1348. <https://doi.org/10.1038/s41588-019-0481-0>.
- Maurano, M.T., Humbert, R., Rynes, E., Thurman, R.E., Haugen, E., Wang, H., Reynolds, A.P., Sandstrom, R., Qu, H., Brody, J., et al. (2012). Systematic localization of common disease-associated variation in regulatory DNA. *Science* *337*, 1190–1195. <https://doi.org/10.1126/science.1222794>.
- Heintzman, N.D., Hon, G.C., Hawkins, R.D., Kheradpour, P., Stark, A., Harp, L.F., Ye, Z., Lee, L.K., Stuart, R.K., Ching, C.W., et al. (2009). Histone modifications at human enhancers reflect global cell-type-specific gene expression. *Nature* *459*, 108–112. <https://doi.org/10.1038/nature07829>.
- Prestel, M., Prell-Schicker, C., Webb, T., Malik, R., Lindner, B., Ziesch, N., Rex-Haffner, M., Röhl, S., Viturawong, T., Lehm, M., et al. (2019). The Atherosclerosis Risk Variant rs2107595 Mediates Allele-Specific Transcriptional Regulation of HDAC9 via E2F3 and Rb1. *Stroke* *50*, 2651–2660. <https://doi.org/10.1161/STROKEAHA.119.026112>.
- Lapierre, M., Linares, A., Dalvai, M., Duraffourd, C., Bonnet, S., Boulahtouf, A., Rodriguez, C., Jalaguier, S., Assou, S., Orsetti, B., et al. (2016). Histone deacetylase 9 regulates breast cancer cell proliferation and the response to histone deacetylase inhibitors. *Oncotarget* *7*, 19693–19708. <https://doi.org/10.18632/oncotarget.7564>.
- Asare, Y., Campbell-James, T.A., Bokov, Y., Yu, L.L., Prestel, M., El Bounkari, O., Roth, S., Megens, R.T.A., Straub, T., Thomas, K., et al. (2020). Histone Deacetylase 9 Activates IKK to Regulate Atherosclerotic Plaque Vulnerability. *Circ. Res.* *127*, 811–823. <https://doi.org/10.1161/circresaha.120.316743>.
- Lecce, L., Xu, Y., V'Gangula, B., Chandel, N., Pothula, V., Caudrillier, A., Santini, M.P., d'Escamard, V., Ceholski, D.K., Gorski, P.A., et al. (2021). Histone deacetylase 9 promotes endothelial-mesenchymal transition and an unfavorable atherosclerotic plaque phenotype. *J. Clin. Invest.* *131*, e131178. <https://doi.org/10.1172/JCI131178>.
- Lino Cardenas, C.L., Kessinger, C.W., Cheng, Y., MacDonald, C., MacGillivray, T., Ghoshhajra, B., Huleihel, L., Nuri, S., Yeri, A.S., Jaffer, F.A., et al. (2018). An HDAC9-MALAT1-BRG1 complex mediates smooth muscle dysfunction in thoracic aortic aneurysm. *Nat. Commun.* *9*, 1009. <https://doi.org/10.1038/s41467-018-03394-7>.
- Li, X., Zhang, Q., Ding, Y., Liu, Y., Zhao, D., Zhao, K., Shen, Q., Liu, X., Zhu, X., Li, N., et al. (2016). Methyltransferase Dnmt3a upregulates HDAC9 to deacetylate the kinase TBK1 for activation of antiviral innate immunity. *Nat. Immunol.* *17*, 806–815. <https://doi.org/10.1038/ni.3464>.
- Davis, C.A., Hitz, B.C., Sloan, C.A., Chan, E.T., Davidson, J.M., Gabdank, I., Hilton, J.A., Jain, K., Baymuradov, U.K., Narayanan, A.K., et al. (2018). The Encyclopedia of DNA elements (ENCODE): data portal update. *Nucleic Acids Res.* *46*, D794–D801. <https://doi.org/10.1093/nar/gkx1081>.
- Lobera, M., Madauss, K.P., Pohlhaus, D.T., Wright, Q.G., Trocha, M., Schmidt, D.R., Baloglu, E., Trump, R.P., Head, M.S., Hofmann, G.A., et al. (2013). Selective class IIa histone deacetylase inhibition via a non-chelating zinc-binding group. *Nat. Chem. Biol.* *9*, 319–325. <https://doi.org/10.1038/nchembio.1223>.
- Dick, M.S., Sborgi, L., Rühl, S., Hiller, S., and Broz, P. (2016). ASC filament formation serves as a signal amplification mechanism for inflammasomes. *Nat. Commun.* *7*, 11929. <https://doi.org/10.1038/ncomms11929>.
- Wang, L., de Zoeten, E.F., Greene, M.I., and Hancock, W.W. (2009). Immunomodulatory effects of deacetylase inhibitors: therapeutic targeting of FOXP3+ regulatory T cells. *Nat. Rev. Drug Discov.* *8*, 969–981.
- Asare, Y., Shnipova, M., Živković, L., Schlegl, C., Tosato, F., Aronova, A., Brandhofer, M., Strohm, L., Beaufort, N., Malik, R., et al. (2022). IKKbeta binds NLRP3 providing a shortcut to inflammasome activation for rapid immune responses. *Signal Transduct. Target. Ther.* *7*, 355. <https://doi.org/10.1038/s41392-022-01189-3>.

28. Schmacke, N.A., O'Duill, F., Gaidt, M.M., Szymanska, I., Kamper, J.M., Schmid-Burgk, J.L., Mädler, S.C., Mackens-Kiani, T., Kozaki, T., Chauhan, D., et al. (2022). IKKbeta primes inflammasome formation by re-cruiting NLRP3 to the trans-Golgi network. *Immunity* 55, 2271–2284.e7. <https://doi.org/10.1016/j.immuni.2022.10.021>.
29. Daniel, B., Belk, J.A., Meier, S.L., Chen, A.Y., Sandor, K., Czimmerer, Z., Varga, Z., Bene, K., Buquicchio, F.A., Qi, Y., et al. (2023). Macrophage inflammatory and regenerative response periodicity is programmed by cell cycle and chromatin state. *Mol. Cell* 83, 121–138.e7. <https://doi.org/10.1016/j.molcel.2022.11.017>.
30. Zhang, Y., Yang, Y., Yang, F., Liu, X., Zhan, P., Wu, J., Wang, X., Wang, Z., Tang, W., Sun, Y., et al. (2023). HDAC9-mediated epithelial cell cycle arrest in G2/M contributes to kidney fibrosis in male mice. *Nat. Commun.* 14, 3007. <https://doi.org/10.1038/s41467-023-38771-4>.
31. Shah, M.H., Binkley, P., Chan, K., Xiao, J., Arbogast, D., Collamore, M., Farra, Y., Young, D., and Grever, M. (2006). Cardiotoxicity of histone deacetylase inhibitor depsipeptide in patients with metastatic neuroendocrine tumors. *Clin. Cancer Res.* 12, 3997–4003. <https://doi.org/10.1158/1078-0432.CCR-05-2689>.
32. Zhao, Z., Ukidve, A., Kim, J., and Mitragotri, S. (2020). Targeting Strategies for Tissue-Specific Drug Delivery. *Cell* 181, 151–167. <https://doi.org/10.1016/j.cell.2020.02.001>.
33. Duivenvoorden, R., Senders, M.L., van Leent, M.M.T., Pérez-Medina, C., Nahrendorf, M., Fayad, Z.A., and Mulder, W.J.M. (2019). Nanoimmunotherapy to treat ischaemic heart disease. *Nat. Rev. Cardiol.* 16, 21–32. <https://doi.org/10.1038/s41569-018-0073-1>.
34. Duivenvoorden, R., Tang, J., Cormode, D.P., Mieszawska, A.J., Izquierdo-Garcia, D., Ozcan, C., Otten, M.J., Zaidi, N., Lobatto, M.E., van Rijs, S.M., et al. (2014). A statin-loaded reconstituted high-density lipoprotein nanoparticle inhibits atherosclerotic plaque inflammation. *Nat. Commun.* 5, 3065. <https://doi.org/10.1038/ncomms4065>.
35. Georgakakis, M.K., Bernhagen, J., Heitman, L.H., Weber, C., and Dichgans, M. (2022). Targeting the CCL2-CCR2 axis for atheroprotection. *Eur. Heart J.* 43, 1799–1808. <https://doi.org/10.1093/eurheartj/ehac094>.
36. Tardif, J.C., Kouz, S., Waters, D.D., Bertrand, O.F., Diaz, R., Maggioni, A.P., Pinto, F.J., Ibrahim, R., Gamra, H., Kiwan, G.S., et al. (2019). Efficacy and Safety of Low-Dose Colchicine after Myocardial Infarction. *N. Engl. J. Med.* 381, 2497–2505. <https://doi.org/10.1056/NEJMoa1912388>.
37. Nidorf, S.M., Fiolet, A.T.L., Mosterd, A., Eikelboom, J.W., Schut, A., Opstal, T.S.J., The, S.H.K., Xu, X.F., Ireland, M.A., Lenderink, T., et al. (2020). Colchicine in Patients with Chronic Coronary Disease. *N. Engl. J. Med.* 383, 1838–1847. <https://doi.org/10.1056/NEJMoa2021372>.
38. Gomez, D., Baylis, R.A., Durgin, B.G., Newman, A.A.C., Alencar, G.F., Mahan, S., St Hilaire, C., Müller, W., Waisman, A., Francis, S.E., et al. (2018). Interleukin-1beta has atheroprotective effects in advanced atherosclerotic lesions of mice. *Nat. Med.* 24, 1418–1429. <https://doi.org/10.1038/s41591-018-0124-5>.
39. Hindorf, L.A., Sethupathy, P., Junkins, H.A., Ramos, E.M., Mehta, J.P., Collins, F.S., and Manolio, T.A. (2009). Potential etiologic and functional implications of genome-wide association loci for human diseases and traits. *Proc. Natl. Acad. Sci. USA* 106, 9362–9367. <https://doi.org/10.1073/pnas.0903103106>.
40. Thomas, E.D., Timms, A.E., Giles, S., Harkins-Perry, S., Lyu, P., Hoang, T., Qian, J., Jackson, V.E., Bahlo, M., Blackshaw, S., et al. (2022). Cell-specific cis-regulatory elements and mechanisms of non-coding genetic disease in human retina and retinal organoids. *Dev. Cell* 57, 820–836.e6. <https://doi.org/10.1016/j.devcel.2022.02.018>.
41. Turner, A.W., Hu, S.S., Mosquera, J.V., Ma, W.F., Hodonsky, C.J., Wong, D., Auguste, G., Song, Y., Sol-Church, K., Farber, E., et al. (2022). Single-nucleus chromatin accessibility profiling highlights regulatory mechanisms of coronary artery disease risk. *Nat. Genet.* 54, 804–816. <https://doi.org/10.1038/s41588-022-01069-0>.
42. Musunuru, K., Strong, A., Frank-Kamenetsky, M., Lee, N.E., Ahfeldt, T., Sachs, K.V., Li, X., Li, H., Kuperwasser, N., Ruda, V.M., et al. (2010). From noncoding variant to phenotype via SORT1 at the 1p13 cholesterol locus. *Nature* 466, 714–719. <https://doi.org/10.1038/nature09266>.
43. Gupta, R.M., Hadaya, J., Trehan, A., Zekavat, S.M., Roselli, C., Klarin, D., Emdin, C.A., Hilvering, C.R.E., Bianchi, V., Mueller, C., et al. (2017). A Genetic Variant Associated with Five Vascular Diseases Is a Distal Regulator of Endothelin-1 Gene Expression. *Cell* 170, 522–533.e15. <https://doi.org/10.1016/j.cell.2017.06.049>.
44. Kundaje, A., Meuleman, W., Ernst, J., Bilenky, M., Yen, A., Heravi-Moussavi, A., Kheradpour, P., Zhang, Z., Wang, J., et al.; Roadmap Epigenomics Consortium (2015). Integrative analysis of 111 reference human epigenomes. *Nature* 518, 317–330. <https://doi.org/10.1038/nature14248>.
45. Heinz, S., Romanoski, C.E., Benner, C., Allison, K.A., Kaikkonen, M.U., Orozco, L.D., and Glass, C.K. (2013). Effect of natural genetic variation on enhancer selection and function. *Nature* 503, 487–492. <https://doi.org/10.1038/nature12615>.
46. He, M., Chiang, H.H., Luo, H., Zheng, Z., Qiao, Q., Wang, L., Tan, M., Ohkubo, R., Mu, W.C., Zhao, S., et al. (2020). An Acetylation Switch of the NLRP3 Inflammasome Regulates Aging-Associated Chronic Inflammation and Insulin Resistance. *Cell Metab.* 31, 580–591.e5. <https://doi.org/10.1016/j.cmet.2020.01.009>.
47. Guan, C., Huang, X., Yue, J., Xiang, H., Shaheen, S., Jiang, Z., Tao, Y., Tu, J., Liu, Z., Yao, Y., et al. (2021). SIRT3-mediated deacetylation of NLRC4 promotes inflammasome activation. *Theranostics* 11, 3981–3995. <https://doi.org/10.7150/thno.55573>.
48. Stutz, A., Kolbe, C.C., Stahl, R., Horvath, G.L., Franklin, B.S., van Ray, O., Brinkschulte, R., Geyer, M., Meissner, F., and Latz, E. (2017). NLRP3 inflammasome assembly is regulated by phosphorylation of the pyrin domain. *J. Exp. Med.* 214, 1725–1736. <https://doi.org/10.1084/jem.20160933>.
49. Swanson, K.V., Deng, M., and Ting, J.P.Y. (2019). The NLRP3 inflammasome: molecular activation and regulation to therapeutics. *Nat. Rev. Immunol.* 19, 477–489. <https://doi.org/10.1038/s41577-019-0165-0>.
50. Khyzha, N., Alizada, A., Wilson, M.D., and Fish, J.E. (2017). Epigenetics of Atherosclerosis: Emerging Mechanisms and Methods. *Trends Mol. Med.* 23, 332–347. <https://doi.org/10.1016/j.molmed.2017.02.004>.
51. Choi, J.H., Nam, K.H., Kim, J., Baek, M.W., Park, J.E., Park, H.Y., Kwon, H.J., Kwon, O.S., Kim, D.Y., and Oh, G.T. (2005). Trichostatin A exacerbates atherosclerosis in low density lipoprotein receptor-deficient mice. *Arterioscler. Thromb. Vasc. Biol.* 25, 2404–2409. <https://doi.org/10.1161/01.ATV.0000184758.07257.88>.
52. Van den Bossche, J., Neele, A.E., Hoeksema, M.A., de Heij, F., Boshuizen, M.C.S., van der Velden, S., de Boer, V.C., Reedquist, K.A., and de Winther, M.P.J. (2014). Inhibiting epigenetic enzymes to improve atherogenic macrophage functions. *Biochem. Biophys. Res. Commun.* 455, 396–402. <https://doi.org/10.1016/j.bbrc.2014.11.029>.
53. Zhang, C.L., McKinsey, T.A., Chang, S., Antos, C.L., Hill, J.A., and Olson, E.N. (2002). Class II histone deacetylases act as signal-responsive repressors of cardiac hypertrophy. *Cell* 110, 479–488. [https://doi.org/10.1016/s0092-8674\(02\)00861-9](https://doi.org/10.1016/s0092-8674(02)00861-9).
54. Azghandi, S., Prell, C., van der Laan, S.W., Schneider, M., Malik, R., Berer, K., Gerdes, N., Pasterkamp, G., Weber, C., Haffner, C., et al. (2015). Deficiency of the stroke relevant HDAC9 gene attenuates atherosclerosis in accord with allele-specific effects at 7p21.1. *Stroke* 46, 197–202. <https://doi.org/10.1161/STROKEAHA.114.007213>.
55. Fernandes-Alnemri, T., Yu, J.W., Datta, P., Wu, J., and Alnemri, E.S. (2009). AIM2 activates the inflammasome and cell death in response to cytoplasmic DNA. *Nature* 458, 509–513. <https://doi.org/10.1038/nature07710>.
56. Hornung, V., Ablasser, A., Charrel-Dennis, M., Bauernfeind, F., Horvath, G., Caffrey, D.R., Latz, E., and Fitzgerald, K.A. (2009). AIM2 recognizes cytosolic dsDNA and forms a caspase-1-activating inflammasome with ASC. *Nature* 458, 514–518. <https://doi.org/10.1038/nature07725>.
57. Cox, J., and Mann, M. (2008). MaxQuant enables high peptide identification rates, individualized p.p.b.-range mass accuracies and

- proteome-wide protein quantification. *Nat. Biotechnol.* 26, 1367–1372. <https://doi.org/10.1038/nbt.1511>.
58. Dobin, A., Davis, C.A., Schlesinger, F., Drenkow, J., Zaleski, C., Jha, S., Batut, P., Chaisson, M., and Gingeras, T.R. (2013). STAR: ultrafast universal RNA-seq aligner. *Bioinformatics* 29, 15–21. <https://doi.org/10.1093/bioinformatics/bts635>.
59. Love, M.I., Huber, W., and Anders, S. (2014). Moderated estimation of fold change and dispersion for RNA-seq data with DESeq2. *Genome Biol.* 15, 550. <https://doi.org/10.1186/s13059-014-0550-8>.
60. Schindelin, J., Arganda-Carreras, I., Frise, E., Kaynig, V., Longair, M., Pietzsch, T., Preibisch, S., Rueden, C., Saalfeld, S., Schmid, B., et al. (2012). Fiji: an open-source platform for biological-image analysis. *Nat. Methods* 9, 676–682. <https://doi.org/10.1038/nmeth.2019>.
61. Georgakis, M.K., van der Laan, S.W., Asare, Y., Mekke, J.M., Haitjema, S., Schoneveld, A.H., de Jager, S.C.A., Nurmohamed, N.S., Kroon, J., Stroes, E.S.G., et al. (2021). Monocyte-Chemoattractant Protein-1 Levels in Human Atherosclerotic Lesions Associate With Plaque Vulnerability. *Arterioscler. Thromb. Vasc. Biol.* 41, 2038–2048.
62. Verhoeven, B.A.N., Velema, E., Schoneveld, A.H., de Vries, J.P.P.M., de Bruin, P., Seldenrijk, C.A., de Kleijn, D.P.V., Busser, E., van der Graaf, Y., Moll, F., et al. (2004). Athero-express: differential atherosclerotic plaque expression of mRNA and protein in relation to cardiovascular events and patient characteristics. Rationale and design. *Eur. J. Epidemiol.* 19, 1127–1133. <https://doi.org/10.1007/s10564-004-2304-6>.
63. Toole, J.F. (1996). ACAS recommendations for carotid endarterectomy. ACAS Executive Committee. *Lancet* 347, 121. [https://doi.org/10.1016/s0140-6736\(96\)90246-9](https://doi.org/10.1016/s0140-6736(96)90246-9).
64. Coyne, T.J., and Wallace, M.C. (1994). Surgical referral for carotid artery stenosis—the influence of NASCET. North American Symptomatic Carotid Endarterectomy Trial. *Can. J. Neurol. Sci.* 21, 129–132. <https://doi.org/10.1017/s0317167100049052>.
65. Hellings, W.E., Peeters, W., Moll, F.L., Piers, S.R.D., van Setten, J., Van der Spek, P.J., de Vries, J.P.P.M., Seldenrijk, K.A., De Bruin, P.C., Vink, A., et al. (2010). Composition of carotid atherosclerotic plaque is associated with cardiovascular outcome: a prognostic study. *Circulation* 121, 1941–1950. <https://doi.org/10.1161/CIRCULATIONAHA.109.887497>.
66. Bentzon, J.F., Otsuka, F., Virmani, R., and Falk, E. (2014). Mechanisms of plaque formation and rupture. *Circ. Res.* 114, 1852–1866. <https://doi.org/10.1161/CIRCRESAHA.114.302721>.
67. Wefers, B., Wurst, W., and Kühn, R. (2023). Gene Editing in Mouse Zygotes Using the CRISPR/Cas9 System. *Methods Mol. Biol.* 2631, 207–230. [https://doi.org/10.1007/978-1-0716-2990-1\\_8](https://doi.org/10.1007/978-1-0716-2990-1_8).
68. Singer, M., Simon, K., Forné, I., and Meissner, M. (2023). A central CRMP complex essential for invasion in *Toxoplasma gondii*. *PLoS Biol.* 21, e3001937. <https://doi.org/10.1371/journal.pbio.3001937>.
69. Perez-Riverol, Y., Bai, J., Bandla, C., García-Seisdedos, D., Hewapathirana, S., Kamatchinathan, S., Kundu, D.J., Prakash, A., Frericks-Zipper, A., Eisenacher, M., et al. (2022). The PRIDE database resources in 2022: a hub for mass spectrometry-based proteomics evidences. *Nucleic Acids Res.* 50, D543–D552. <https://doi.org/10.1093/nar/gkab1038>.
70. Brandhofer, M., Hoffmann, A., Blanchet, X., Siminkovitch, E., Rohlfing, A.K., El Bounkari, O., Nestele, J.A., Bild, A., Kontos, C., Hille, K., et al. (2022). Heterocomplexes between the atypical chemokine MIF and the CXCR4-motif chemokine CXCL4L1 regulate inflammation and thrombus formation. *Cell. Mol. Life Sci.* 79, 512. <https://doi.org/10.1007/s00018-022-04539-0>.
71. Kontos, C., El Bounkari, O., Krammer, C., Sinitzki, D., Hille, K., Zan, C., Yan, G., Wang, S., Gao, Y., Brandhofer, M., et al. (2020). Designed CXCR4 mimic acts as a soluble chemokine receptor that blocks atherogenic inflammation by agonist-specific targeting. *Nat. Commun.* 11, 5981. <https://doi.org/10.1038/s41467-020-19764-z>.
72. Swamy, M., Siegers, G.M., Minguet, S., Wollscheid, B., and Schamel, W.W.A. (2006). Blue native polyacrylamide gel electrophoresis (BN-PAGE) for the identification and analysis of multiprotein complexes. *Sci. STKE* 2006, pl4. <https://doi.org/10.1126/stke.3452006pl4>.
73. He, Y., Zeng, M.Y., Yang, D., Motro, B., and Núñez, G. (2016). NEK7 is an essential mediator of NLRP3 activation downstream of potassium efflux. *Nature* 530, 354–357. <https://doi.org/10.1038/nature16959>.
74. Lugin, J., and Martinon, F. (2017). Detection of ASC Oligomerization by Western Blotting. *Bio Protoc.* 7, e2292. <https://doi.org/10.21769/BioProtoc.2292>.
75. Cao, J., Roth, S., Zhang, S., Kopczak, A., Mami, S., Asare, Y., Georgakis, M.K., Messerer, D., Horn, A., Shemer, R., et al. (2024). DNA-sensing inflammasomes cause recurrent atherosclerotic stroke. *Nature* 633, 433–441. <https://doi.org/10.1038/s41586-024-07803-4>.

**STAR★METHODS**

**KEY RESOURCES TABLE**

REAGENT or RESOURCE	SOURCE	IDENTIFIER
<b>Antibodies</b>		
Acetylated-Lysine Antibody	Cell Signaling Technology	Cat# 9441; RRID:AB_331805
Alexa Fluor® 488 anti-mouse CD117 (c-Kit) Antibody	Biolegend	Cat#105815;RRID:AB_493473
Anti-Actin	Sigma-Aldrich	Cat#A2066; RRID:AB_476693
Anti-Actin, $\alpha$ -Smooth Muscle - Cy3™ antibody, Mouse monoclonal	Sigma-Aldrich	Cat# C6198; RRID:AB_476856
Anti-Asc (AL177)	AdipoGen Life Sciences	Cat# AG-25B-0006-C100; RRID: AB_2490440
Anti-Caspase-1 (p20) (human) mAb	AdipoGen Life Sciences	Cat# AG-20B-0048-C100; RRID: AB_2490257
Anti-Caspase-1 (p20) (mouse) mAb (Casper-1)	AdipoGen Life Sciences	Cat# AG-20B-0042-C100; RRID: AB_2490248
Anti-CD68 antibody	Abcam	Cat#125212; RRID:AB_10975465
Anti-mouse CD11b Monoclonal Antibody (M1/70) PerCP-Cyanine5.5	Thermo Fisher Scientific	Cat# 45-0112-82;RRID:AB_953558
Anti-mouse CD11c Monoclonal Antibody (N418) PE-Cyanine7	Thermo Fisher Scientific	Cat# 25-0114-82; RRID:AB_469590
Anti-mouse CD3e Monoclonal Antibody (145-2C11) FITC	Thermo Fisher Scientific	Cat# 11-0031-82;RRID:AB_464882
Anti-human HDAC9 antibody	Thermo Fisher Scientific	Cat#MA5-32820; RRID:AB_2810096
Anti-mouse CD45 Monoclonal Antibody (30-F11) eFluor™ 450	Thermo Fisher Scientific	Cat# 48-0451-82;RRID:AB_1518806
Anti-Mouse/Human Mac-2 (Galectin-3) Antibody	Cedarlane Labs	Cat#CL8942AP; RRID:AB_10060357
Anti-NLRP3/NALP3 mAb (Cryo-2)	AdipoGen Life Sciences	Cat# AG-20B-0014-C100;RRID: AB_2490202
APC anti-mouse CD16/32 Antibody	Biolegend	Cat# 101325;RRID:AB_1953272
APC-H7 Mouse Anti-Human CD4	BD Bioscience	Cat#560251; RRID:AB_1645477
CD44 Monoclonal Antibody (IM7), APC	Thermo Fisher Scientific	Cat#17-0441-82; RRID:AB_469390
CD62L (L-Selectin) Monoclonal Antibody (MEL-14), PE-Cyanine7	Thermo Fisher Scientific	Cat# 25-0621-82;RRID:AB_469633
CD8a Monoclonal Antibody (53-6.7), eFluor™ 450	Thermo Fisher Scientific	Cat# 48-0081-82;RRID:AB_1272198
Cy3-conjugated AffiniPure Donkey anti-rabbit IgG (H+L)	Jackson ImmunoResearch	Cat# 11473299;RRID:AB_2307443
Gasdermin D (E9S1X) Rabbit mAb	Cell Signaling Technology	Cat# 39754; RRID:AB_2916333
Goat anti-Mouse IgG (H+L) Secondary Antibody HRP	Thermo Fisher Scientific	Cat# 31430; RRID:AB_228307
HA-Tag (C29F4) Rabbit mAb	Cell Signaling Technology	Cat# 3724S; RRID:AB_1549585
Ly-6C Antibody anti-mouse APC	Miltenyi	Cat# 130-123-796;RRID:AB_2857638
Monoclonal ANTI-FLAG® M2 antibody produced in mouse	Sigma-Aldrich	Cat# F3165-1MG;RRID:AB_259529
Mouse IgG2b Isotype Control	AdipoGen Life Sciences	Cat# AG-35B-0005-C050;RRID: AB_3665690
Myc-Tag (9B11) Mouse mAb	Cell Signaling Technology	Cat# 2276S; RRID:AB_331783
PE Rat Anti-Mouse Ly-6G clone 1A8	BD Bioscience	Cat# 551461; RRID:AB_394208
V5-Tag (D3H8Q) Rabbit mAb	Cell Signaling Technology	Cat# 13202; RRID:AB_2687461
<b>Chemicals, peptides, and recombinant proteins</b>		
Anilinblau (MASSON C)	MORPHISTO	Cat# 10141.02500
Oil Red O solution 0.5% in propylene glycol	Sigma-Aldrich	Cat# O1516-500ML
Picro-Sirius Red Solution	MORPHISTO	Cat# 13422.00250
PolyFect Transfection Reagent	Qiagen	Cat# 301107
TMP 195, 98.7%	Axon Medchem	Cat# Axon 2180
DAPI	Molecular Probes	Cat# D1306
Weigert's iron hematoxylin solution	Sigma-Aldrich	Cat# HT1079-1SET

(Continued on next page)

**Continued**

REAGENT or RESOURCE	SOURCE	IDENTIFIER
Phosphomolybdic/Phosphotungstic Acid Solution	Biozol	Cat# SCY-PPA999
Biebrich Scarlet / Acid Fuchsin Solution	Scy Tek	Cat# BSU999
Bis-tris	Thermo Fisher	Cat# J12112.A1
Bouin's solution	Sigma-Aldrich	Cat# HT101-32
Bovine serum albumine	Sigma-Aldrich	Cat# A2153-1KG
Cell lysis buffer 10x	Cell Signaling Technology	Cat# 9803
Citric acid	Merck	Cat# 100241
Collagenase Type II	Merck	Cat# C2-22-1G
Complete™ protease inhibitor cocktail	Sigma-Aldrich	Cat# 4693159001
Coomassie blue G250	Sigma-Aldrich	Cat# 27815
Digitonin	Sigma-Aldrich	Cat# D141-500MG
DMSO, Anhydrous	Thermo Fisher Scientific	Cat# D12345
Immobilon Western Chemiluminescent HRP Substrate	Millipore	Cat# WBKLS0500
Immobilon-P Membrane PVDF 045 μm	Millipore	Cat# IPVH00010
Kaisers glycerin-gelatine, phenol-free	Carl Roth	Cat# 6474.1
NativePAGE™ 3 to 12% Bis-Tris 1.0mm Mini Protein Gel 10-well	Invitrogen by Thermo Fisher	Cat# BN1001BOX
Paraformaldehyd (PFA) 4% in PBS 74	MORPHISTO	Cat# 1.176.201.000
Penicillin-Streptomycin (10000 U/mL)	Gibco	Cat# 15140122
Phenylmethylsulfonyl fluoride	Thermo Fisher	Cat# 36978
ROTI®Histokitt	Carl Roth	Cat# 6638.1
Human NLRP3	OriGene Technologies, Inc.,	Cat# TP320952
Human HDAC9	OriGene Technologies, Inc.,	Cat# TP315267
<b>Critical commercial assays</b>		
Abca1 mouse QuantiTect Primer Assay	QIAGEN	Cat# QT00165690
Abcg1 mouse QuantiTect Primer Assay	QIAGEN	Cat# QT00113519
HDAC9 human TaqMan probe	Thermo Fisher Scientific	Cat# 4331182
HDAC9 mouse TaqMan probe	Thermo Fisher Scientific	Cat# 4331182
HPRT mouse TaqMan probe	Thermo Fisher Scientific	Cat# 4448489
TWIST1 mouse TaqMan probe	Thermo Fisher Scientific	Cat# 4331182
Caspase-Glo® 1 Inflammasome Assay	Promega	Cat# G9951
Cholesterol fluorometric assay kit	Cayman Chemical	Cat# 10007640
CyQUANT™ LDH Cytotoxicity Assay	Thermo Fisher Scientific	Cat# C20301
FAM-FLICA® Caspase-1 (YVAD) Assay Kit	ImmunoChemistryTechnologies	Cat# 97
Human IL-1 beta/IL-1F2 Quantikine ELISA Kit	R&D systems	Cat# DLB50
Human Total IL-18/IL-1F4 Quantikine ELISA Kit	R&D systems	Cat# DL180
Mouse IL-1 beta/IL-1F2 DuoSet ELISA	R&D systems	Cat# DY401-05
Mouse IL-18 DuoSet ELISA	R&D systems	Cat# DY7625-05
Omniscrypt RT kit	QIAGEN	Cat# 205113
Human IL-1 beta/IL-1F2 Quantikine ELISA Kit	R&D systems	Cat# DLB50
Human Total IL-18/IL-1F4 Quantikine ELISA Kit	R&D systems	Cat# DL180
Mouse IL-1 beta/IL-1F2 DuoSet ELISA	R&D systems	Cat# DY401-05
Mouse IL-18 DuoSet ELISA	R&D systems	Cat# DY7625-05
Omniscrypt RT kit	QIAGEN	Cat# 205113
Pan B cell isolation kit	Miltenyi Biotec GmbH	Cat# 130-090-862
Pan Monocyte Isolation Kit human	Miltenyi Biotec GmbH	Cat# 130-096-537
Pan T cell isolation kit	Miltenyi Biotec GmbH	Cat# 130-095-130
Pierce™ BCA protein assay kit	Thermo Fisher Scientific	Cat# 23225
Quantinova SYBR green PCR kit	QIAGEN	Cat# 208056

(Continued on next page)

**Continued**

REAGENT or RESOURCE	SOURCE	IDENTIFIER
Th1/Th2 Cytokine & Chemokine 20-Plex Mouse ProcartaPlex™ Panel 1	Thermo Fisher	Cat# EPX200-26090-901
Triglyceride colorimetric assay kit	Cayman Chemical	Cat# 10010303
Zombie NIR™ Fixable Viability Kit	Biolegend	Cat# 423105
RNase-Free DNase Set (50)	QIAGEN	Cat# 79254
RNeasy micro kit	QIAGEN	Cat# 74004
RNeasy mini kit	QIAGEN	Cat# 74104
<b>Deposited data</b>		
Raw and analyzed data	This Paper	<a href="https://doi.org/10.34894/4IKE3T">https://doi.org/10.34894/4IKE3T</a> ; <a href="https://doi.org/10.34894/Q1135J">https://doi.org/10.34894/Q1135J</a> ; <a href="https://doi.org/10.34894/D1MDKL">https://doi.org/10.34894/D1MDKL</a> ; GSE274312, PXD042078
<b>Experimental models: Cell lines</b>		
THP1 monocytes	Abcam	Cat# ab275477
HEK293	ATCC	<a href="https://www.lgcstandards-atcc.org/products/all/CRL-1573.aspx?geo_country=de">https://www.lgcstandards-atcc.org/products/all/CRL-1573.aspx?geo_country=de</a>
<b>Experimental models: Organisms/strains</b>		
<i>Hdac9</i> <sup>-iCRE</sup>	This Paper	N/A
<i>Hdac9</i> <sup>-iCRE</sup> <i>Apoe</i> <sup>-/-</sup>	This Paper	N/A
<i>Apoe</i> <sup>-/-</sup>	The Jackson Laboratory	<a href="https://www.jax.org/strain/002052">https://www.jax.org/strain/002052</a>
<i>Hdac9</i> <sup>LysM</sup> <i>Apoe</i> <sup>-/-</sup>	This Paper	N/A
<i>Hdac9</i> <sup>-/-</sup>	Zhang et al. <sup>53</sup>	<a href="https://www.informatics.jax.org/allele/MGI:2387834">https://www.informatics.jax.org/allele/MGI:2387834</a>
<i>Hdac9</i> <sup>-/-</sup> <i>Apoe</i> <sup>-/-</sup>	Azghandi et al. <sup>54</sup>	N/A
<b>Oligonucleotides</b>		
ON-TARGET plus Non-targeting Pool	Dharmacon	Cat# D-001810-10-05
SMARTpool: ON-TARGET plus <i>Hdac9</i> siRNA	Dharmacon	Cat# L-066143-00-0005
Primers	Table S3	N/A
<b>Recombinant DNA</b>		
pcDNA™6/V5-His-HDAC9	This paper	N/A
Flag-NLRP3	Florian Schmidt	N/A
Flag-NLRP3-ΔPYD	Florian Schmidt	N/A
Flag-NLRP3-LRR	Florian Schmidt	N/A
Flag-NLRP3-NACHT	Florian Schmidt	N/A
Flag-NLRP3-PYD	Florian Schmidt	N/A
Flag-NLRP3-ΔLRR	Florian Schmidt	N/A
Flag-Aim 2	Fernandes-Alnemri et al. <sup>55</sup>	Addgene #51537
Flag-NLRC4	Veit Hornung	N/A
HA-ASC	Hornung et al. <sup>56</sup>	Addgene #41553
Myc-Caspase 1 p45	Hornung et al. <sup>56</sup>	Addgene #41552
<b>Software and algorithms</b>		
AxioVision	Carl Zeiss Microscopy	N/A
ZEN 2.3 lite	Carl Zeiss Microscopy	Blue Edition
BD FACSuite	Beckton Dickinson	N/A
Fusion Fx7	Vilber	N/A
MaxQuant 2.1.0.0	Cox and Mann <sup>57</sup>	RRID:SCR_014485
Monolith™ NT.115 control software	NanoTemper Technologies	N/A
xPONENT	Luminex® Systems	N/A
STAR software, version 2.6.1d	Dobin et al. <sup>58</sup>	RRID:SCR_004463
DESeq2 Bioconductor R package	Love et al. <sup>59</sup>	RRID:SCR_015687
Image J (Fiji)	Schindelin et al. <sup>60</sup>	RRID:SCR_002285

(Continued on next page)

**Continued**

REAGENT or RESOURCE	SOURCE	IDENTIFIER
MO.AffinityAnalysis V2.3	NanoTemper Technologies	N/A
GraphPad Prism 10	GraphPad SoftwareInc	N/A
Ingenuity Pathway Analysis	QIAGEN	<a href="https://digitalinsights.qiagen.com/IPA">https://digitalinsights.qiagen.com/IPA</a>
<b>Other</b>		
Lipopolysaccharide from Escherichia coli O111:B4	Sigma-Aldrich	Cat# L2630-10MG
Nigericin Sodium Salt	Tocris	Cat# 4312
Dynabeads™ Protein G for Immunoprecipitation	Thermo Fisher Scientific	Cat# 10004D
CD14 microbeads human	Miltenyi	Cat# 130-050-201
1 kb plus DNA ladder	Bioline	Cat# BIO-33053

**EXPERIMENTAL MODEL AND STUDY PARTICIPANT DETAILS****Human atherosclerosis study subjects**

The study population for human atherosclerosis investigations was recently reported.<sup>61</sup> We used data from the Athero-Express Biobank, an ongoing prospective study of patients undergoing endarterectomy for manifestations of atherosclerosis.<sup>62</sup> Carotid endarterectomy was performed following recommendations by the ACAS (Asymptomatic Carotid Atherosclerosis Study)<sup>63</sup> and The NASCET (North American Symptomatic Carotid Endarterectomy Trial).<sup>64</sup> Patients were recruited from the St. Antonius Hospital Nieuwegein and University Medical Center Utrecht in Utrecht, the Netherlands between 2002 and 2019. Individuals who agreed to participate completed questionnaires about medical history and medication use before the operation and provided blood samples for biochemical and hematologic analyses. Their plaque samples were postoperatively collected and analyzed as described below. Individuals were included in the current study based on having undergone carotid endarterectomy and available measurements of *HDAC9* expression in plaque. The study protocol conforms to the Declaration of Helsinki and was approved by the ethics committee on research on humans of the University Medical Center Utrecht. All participants provided written informed consent.

**Histopathologic analysis of human atherosclerotic plaque composition**

Following carotid endarterectomy, plaque samples were immediately transferred to the laboratory. Plaques were divided in parallel segments of 5 mm thickness perpendicular to the arterial axis, and the segment with the greatest plaque burden was subjected to histopathologic examination, as previously described.<sup>55</sup> All stained sections were examined microscopically and digitally stored. For the purposes of the current study, we explored 5 plaque traits that are established hallmarks of plaque vulnerability: lipid content, collagen deposition, macrophages, SMCs, and intraplaque hemorrhage.<sup>66</sup> Two independent observers manually scored stainings for these traits using previously defined semi-quantitative methods.<sup>62,65</sup> In brief, plaque lipid content was quantified visually as a percentage of fat deposition to total plaque area with the use of hematoxylin-eosin and picosirius red stains; a large lipid core was defined as lipid content of >10% of the total plaque area. Collagen deposition (picrosirius red staining) was manually classified as absent, minor, moderate, or heavy staining along the entire luminal border. The burden of macrophages and SMCs was assessed by staining with antibodies against CD68 and  $\alpha$ -actin, respectively, and was classified into absent, minor, moderate, or heavy staining. In alternative semi-automated computerized analyses, numbers of macrophages and SMCs were quantified on a continuous scale. Specifically, the stainings were scored as percentage of stained area to total plaque area (AnalySiS version 3.2, Soft Imaging GmbH, Munster, Germany). Intraplaque hemorrhage (hematoxylin-eosin and fibrin staining) was defined as the composite of plaque bleeding at the luminal side of the plaque as a result of plaque disruption and was classified as absent or present. Associations of plaque *HDAC9* expression (1 SD increment) with large lipid core (binary traits) as derived from logistic regression analyses (adjusted for age, sex, hypertension, diabetes, current smoking, LDL (low-density lipoprotein)-C levels at time of operation, use of lipid-lowering agents, use of antiplatelet agents, estimated glomerular filtration rate, body mass index, history of cardiovascular disease, and grade of stenosis). To assess the overall instability traits of the atherosclerotic plaque, a vulnerability index was generated ranging from 0 to 5, as previously described.<sup>66</sup> Specifically, one point was given to each plaque for the following histopathologic features: a lipid core >10%, low collagen load (no/minor), high macrophage burden (moderate/heavy), low SMC burden (no/minor), and presence of intraplaque hemorrhage. The data used for these analyses are available through DataverseNL and the codes used are available through a GitHub repository. Data: Athero-Express clinical data, <https://doi.org/10.34894/4IKE3T>; histological data, <https://doi.org/10.34894/QI135J>; bulk transcriptomics data, <https://doi.org/10.34894/D1MDKL>. Code: [https://github.com/CirculatoryHealth/AE\\_20211201\\_YAW\\_SWVANDERLAAN\\_HDAC9](https://github.com/CirculatoryHealth/AE_20211201_YAW_SWVANDERLAAN_HDAC9).

**Blood sampling from patients with atherosclerosis**

Patients with acute ischemic stroke were recruited in 2022 through the stroke service, Klinikum der Universität München, a tertiary level hospital at Ludwig-Maximilians-Universität (LMU), Munich, Germany. Patients (both males and females) were selected based on the presence of carotid atherosclerosis (carotid artery plaques or carotid artery stenosis) documented by carotid ultrasound.

Whole blood was drawn into EDTA-plasma containers (Sarstedt) using a tourniquet and 21-gauge needles. The study was approved by the local ethics committee of LMU Klinikum and was conducted in accordance with the Declaration of Helsinki as well as institutional guidelines. Written and informed consent was obtained from all subjects.

### Generation of mice lacking the CRE at *Hdac9* (*Hdac9*<sup>ΔCRE</sup>)

To generate *Hdac9*<sup>ΔCRE</sup> mice, we employed CRISPR–Cas9-mediated gene editing in zygotes as previously reported.<sup>67</sup> In brief, pronuclear stage zygotes were obtained by mating C57BL/6 males with superovulated C57BL/6 females. Embryos were then microinjected into the male pronucleus with the rs2107595-containing CRE-specific CRISPR–Cas9 mix consisting of 5 ng/μl SpCas9 mRNA, 2.5 ng/μl sgRNA-up (protospacer AATCACATAAGCTTGATAGT), and 2.5 ng/μl sgRNA-dn (protospacer CTGTTGATGGGCATC GAGGT). After microinjection, zygotes were transferred into pseudopregnant CD-1 foster mice. To exclude additional unwanted modifications, putative off-target sites of the CRE-specific sgRNAs were predicted using the CRISPOR online tool. Genomic DNA from F1 mice was PCR-amplified and verified by Sanger sequencing and did not show additional sequence variation. All mice were handled according to institutional guidelines approved by the animal welfare and use committee of the government of Upper Bavaria and housed in standard cages in a specific pathogen-free facility (21 ± 1 °C, on a 12-h light/dark cycle, with average humidity of around 55%) with ad libitum access to food and water in the animal facility at the Centre for Stroke and Dementia Research.

### Conditional inactivation of *Hdac9* gene in mice

Homologous recombination was induced in embryonic stem (ES) cells using a construct containing 2.1 kb of gDNA, intron 2, and a Neo cassette inserted between FRT sites. *Hdac9* exon 3 was flanked by loxP sites and a 5.8 kb fragment of gDNA was introduced as 3' recombination arm. A correctly targeted ES cell clones were injected into blastocysts to produce a chimeric mouse that transmitted the modified allele through the germ line. A male heterozygous for the targeted allele was bred with a female expressing ubiquitous Flippase (Flp) transgene to produce animals with deletion of the Neo cassette while preserving the loxP sites flanking exon 3. R1/E (129/Sv) embryonic stem cells (ES) were cultured on irradiated mouse embryonic fibroblasts (MEFs) using the ES medium KnockOut DMEM containing 12% fetal calf serum, 2 mM L-glutamine, 1 mM sodium pyruvate, 1% penicillin/streptomycin, 100 μM nonessential amino acids (all Invitrogen), 100 μM β-mercaptoethanol, and leukemia inhibitory factor (LIF). ES cells were electroporated using a BIORAD electroporator (250 V, 500 μF) with 25 μg linearized construct (pKO-Hdac9) and selected with 200 μg/ml Geneticin (G418). *Hdac9* floxed mice were generated by laser assisted (XY-Clone Hamilton Thorne) injection of R1/E (129/Sv) cells into 8-cell stage C57Bl/6NCrl embryos. All manipulations were done in the Transgenic Core Facility of the MPI-CBG, Dresden. Chimaeras were crossed to C57Bl/6NCrl mice and their offspring were screened for germline transmission. C57Bl/6NCrl, Crl:CD1(ICR) mice were purchased from Charles River. All mice were housed in IVC units and maintained on a 12-h dark/12-h light cycle. For the production of eight cell stage embryos, 8-week old females were natural mated. The females were screened for vaginal plugs the next morning (0.5 days post coitum, dpc) and housed until embryos were collected by day 2.5 dpc. Crl:CD1(ICR) females were mated with vasectomized Crl:CD1(ICR) males and used as recipients for injected embryo transfer at 0.5 dpc into the oviduct.

## METHOD DETAILS

### Isolation of human monocytes

Human Peripheral Blood Mononuclear Cells (PBMCs) were isolated from whole blood by Ficoll-Paque (GE Healthcare) density gradient centrifugation and were enriched for monocytes with the Monocyte Isolation Kit II (Miltenyi Biotec) according to manufacturer's recommendation. A cocktail of biotin-conjugated antibodies was used to label non-monocytes. Depletion of these labeled cells resulted in enriched monocytes.

### Mouse model of atherosclerosis

Sample sizes for mouse experiments were determined by SigmaPlot 12.5 with 0.80 statistical power, effect size of 0.45, an expected SD of 0.35, and an  $\alpha$ -error of 0.05 based on previous experiments.<sup>19</sup> Mice were randomly assigned to groups, and data collection and analysis were performed blinded. Data were excluded for mice with broken aortic root valves after sectioning of the heart. Mice had ad libitum access to food and water and were housed in a specific pathogen-free animal facility under a 12-hour light-dark cycle. Experiments started when mice were 6 to 8 weeks old and received a Western-type diet containing 21% fat, 0.15% cholesterol (TD88137; Ssniff). At the end of the experiments, mice were anesthetized using ketamine-xylazine or medetomidine-midazolam-fentanyl. Blood was obtained via cardiac puncture, and the arterial tree was perfused through the left ventricle with 0.9% sterile NaCl. Hearts were either fixed in 4% paraformaldehyde or directly embedded in Tissue-Tek OCT for sectioning and quantification of atherosclerotic lesion sizes. For protein analysis via Western blot, the whole aorta was dissected, flash-frozen, and lysed in RIPA buffer containing complete EDTA-free phosphatase and protease inhibitors (Roche) using a tissue homogenizer. All animal experiments were approved by the Institutional Animal Care Committee of Regierung von Oberbayern (ROB-55.2-2532.Vet\_02-14-187; ROB-55.2.2532.Vet\_02-17-007).

### Bone Marrow Transplantation

Recipient *Apoe*<sup>-/-</sup> mice were exposed to a lethal dose of whole-body irradiation (2 × 6.5 Gy) a day before bone marrow (BM) transplantation and transplanted with bone marrow from *Hdac9*<sup>ΔCRE</sup> *Apoe*<sup>-/-</sup> and control *Hdac9*<sup>+/+</sup> *Apoe*<sup>-/-</sup> donors. Irradiated mice were allowed to recuperate for 4 weeks on antibiotics before receiving Western-type diet for 12 weeks.

### Formulating and characterizing TMP195-loaded nanobiologics

TMP195 (4.0 mg, 8.8 μmol, Axon Medchem), 1-myristoyl-2-hydroxy-sn-glycerophosphocholine (MHPC, 5.90 mg, 12.6 μmol, Avanti Polar Lipids), and 1,2-dimyristoyl-sn-glycero-3-phosphatidylcholine (DMPC, 51.2 mg, 75.5 μmol, Avanti Polar Lipids) were dissolved in a chloroform/ethanol solution (90/10 vol.%, 3.0 mL total). The solution was dried under a vacuum to create a thin lipid film. Apolipoprotein A1 (22.8 mg, isolated from human HDL concentration, Biosource Technology) in PBS (12.0 mL) was added to the lipid film. The mixture was incubated at 37 °C for 1 hour and sonicated in a bath sonicator for 5 minutes to form a cloudy suspension. The suspension was sonicated for 20 minutes at 4 °C using a tip sonicator (150 V/T ultrasonic operating at 70% power output) to form crude TMP195-loaded nanobiologics (TMP195-NB). The nanobiologics were concentrated by centrifugal filtration (Vivaspin, 100 kD MWCO) at 4°C and 4000 rpm to a volume of 1.0 mL. PBS (4.0 mL) was added and the solution was again concentrated to 1.0 mL, and this washing step was repeated twice. The final solution was filtered through a syringe filter (PES, 0.22 μm) to obtain pure TMP195-NB as an opaque solution. Nanobiologic sizes were assessed using a Brookhaven ZetaPALS analyzer after diluting an aliquot (20 μL) with PBS (1.0 mL) and filtering this through a syringe filter (PES, 0.22 μm). The nanobiologics' number average mean size was 19.3 ± 5.7 nm and their PDI 0.241 ± 0.045, n=4. TMP195 loading efficiency was determined by HPLC-UV using a C18 column and H<sub>2</sub>O/ACN as the eluent, incorporation efficiencies were 53.5 ± 3.5%, n=2. Unloaded nanobiologics (placebo) were made in an identical fashion, but without TMP-195.

### Treatment of atherosclerosis with the inhibitor MCC950 or TMP195-nanobiologics

*Hdac9*<sup>ΔCRE</sup> *Apoe*<sup>-/-</sup> mice receiving atherogenic diet for 8 weeks were treated with the NLRP3 inhibitor MCC950 (10 mg/kg) three times a week in parallel with the diet feeding. Control *Hdac9*<sup>+/+</sup> *Apoe*<sup>-/-</sup> and *Hdac9*<sup>ΔCRE</sup> *Apoe*<sup>-/-</sup> mice were also placed on Western-type diet for 8 weeks and received PBS as vehicle control. To study the effects of TMP195-NB on already established plaques, *Apoe*<sup>-/-</sup> mice were fed a Western-type diet for 8 weeks and starting in the fifth week, received i.v injections of TMP195-NB (10 mg/kg) or placebo twice a week. Analysis of atherosclerotic plaque size and further characterization were performed as below.

### Immunohistochemistry

The extent of atherosclerosis was assessed in the aortic root by staining lipid depositions with Oil Red O. Hearts were embedded in Tissue-Tek for cryosectioning. Atherosclerotic plaques were quantified in 5-μm or 8-μm transverse serial sections and averages calculated from 3 to 5 sections. Masson trichrome and Picro-sirius red staining was performed on both aortic root and paraffin-embedded aortic arch sections to analyze lesion size, collagen content, fibrous cap thickness, and necrotic core formation. Macrophages and smooth muscle cells were visualized by immunofluorescent staining for Cd68 (cluster of differentiation; Sigma) or Mac2 (Cedarlane) followed by Alexa 488-conjugated affinity purified antibody (Jackson ImmunoResearch) and Sma-cy3 (Sigma), respectively. Nuclei were counterstained by 4',6-diamidino-2-phenylindol. Incubation with secondary antibody alone served as a negative control. All images were recorded with a Zeiss microscope with AxioVision and ZEN 2.3 software, and quantification of lesion size and composition was performed using Image J analysis software.

### Cell lysis, co-immunoprecipitation and Western blot analysis

For total cell lysates, cells were washed with cold PBS and lysed either directly with 1x NuPAGE-LDS-sample buffer (Invitrogen) containing 1 mmol/l DTT (Sigma Aldrich) or with 1x cell lysis buffer (#9803, Cell signaling) containing 20 mM Tris-HCl (pH 7.5), 150 mM NaCl, 1 mM Na<sub>2</sub>EDTA, 1 mM EGTA, 1% Triton, 2.5 mM sodium pyrophosphate, 1 mM beta-glycerophosphate, 1 mM Na<sub>3</sub>VO<sub>4</sub>, 1 μg/mL leupeptin. Protease and phosphatase inhibitors (Roche) were added to all buffers. For immunoprecipitation experiments, HEK293 cells were transiently co-transfected with V5-tagged full-length HDAC9 and Flag-tagged full-length or mutants of NLRP3 (ΔPYD, LRR, NACHT, PYD, and ΔLRR domains; all kindly donated by Dr. Florian Schmidt). Further co-transfections involved the use of Flag-NLRC4 (kindly donated by Dr. Veit Hornung), Flag-AIM2, Flag-ASC, and Flag-Caspase-1 p45. Endogenous interactions were assessed in human THP1 macrophages stimulated with LPS (200 ng/ml, 6 h) and nigericin (5 μM, 60 min). Cell lysates were precleared with Protein A or G beads. Following incubation of lysates with primary antibodies (anti-Flag, anti-V5, or anti-NLRP3) overnight at 4°C, the ensuing protein complexes were incubated with protein A or G beads for 2 h. Antibody-antigen complexes were eluted from the beads after washing three times with 1x cell lysis buffer containing 150 mM NaCl and a final stringent wash with 250 mM NaCl for two times. Total cell lysates or coimmunoprecipitated proteins were separated by SDS-PAGE, transferred to a PVDF membrane (Bio-Rad), and detected with the appropriate antibodies. Primary antibodies were incubated overnight at 4°C. HRP-conjugated anti-mouse or anti-rabbit antibodies were used as secondary antibodies and blots were developed with Immobilon Western HRP Substrate (Merck Millipore). Protein bands were visualized with a Fusion Fx7 and quantified using Image J 1.47v software (Wayne Rasband).

### LC-MS/MS analysis

To verify the interaction between HDAC9 and NLRP3, whole cell extracts from HEK293 cells co-transfected with V5-HDAC9 and Flag-NLRP3 or V5-Empty vector and Flag-NLRP3 was incubated with anti-Flag antibody to purify NLRP3. Following three times

washing with 50 mM  $\text{NH}_4\text{HCO}_3$ , immunoprecipitated Flag-NLRP3 was subjected to LC-MS/MS analysis as described elsewhere<sup>68</sup> with minor changes. MaxQuant 2.1.0.0 was used to identify proteins and quantify by iBAQ with the following parameters: Database UP000000589\_10090\_Mmusculus\_20210405.fasta; MS tol, 10 ppm; MS/MS tol, 20 ppm Da; Peptide FDR, 0.1; Protein FDR, 0.01 min; Peptide Length, 7; Variable modifications, Oxidation (M); Fixed modifications, Carbamidomethyl (C); Peptides for protein quantitation, razor and unique; Min. peptides, 1; Min. ratio count, 2. Identified proteins were considered as interaction partners of the bait if their MaxQuant iBAQ values were > 1.8. The mass spectrometry proteomics data have been deposited to the ProteomeXchange Consortium via the PRIDE<sup>69</sup> partner repository with the dataset identifier PXD042078.

### Microscale thermophoresis (MST) measurements

Protein-protein interactions between HDAC9 and fluorescently labeled NLRP3 were analyzed via microscale thermophoresis (MST) on a Monolith NT.115 instrument equipped with green/red filters (NanoTemper Technologies GmbH, Munich, Germany). Recombinant human NLRP3 (OriGene Technologies, Inc, Rockville, USA) was fluorescently labeled using the Monolith Protein Labeling Kit RED-NHS 2<sup>nd</sup> Generation from NanoTemper (Munich, Germany) according to the manufacturers' instructions. Experiments were performed in a similar manner as reported previously.<sup>27,70,71</sup> Measurements were performed in standard Monolith™ NT.115 series capillaries at 25°C with 40% MST power and 85 % LED excitation power to obtain an initial fluorescence count in the range of 360–460. MST traces were recorded for 40 s (-5 s to +35 s), at default settings with the sample being heated between 0 s and 30 s. All measurements were performed in MST assay buffer (50 mM Tris-HCl, pH 7.4, 150 mM NaCl, 10 mM  $\text{MgCl}_2$ , 0.05% Tween-20). MST-Red-NLRP3 was used at a fixed concentration of 30 nM and mixed with equal volumes of serial dilutions of recombinant human HDAC9 (OriGene Technologies, Inc, Rockville, USA), resulting in a final NLRP3 concentration of 15 nM. Two individual sets of serial dilutions of HDAC9 were prepared and measured in duplicates, resulting in four analyzed MST traces per HDAC9 concentration. Prior to loading into capillaries for measurement, the prepared samples were incubated for at least 40 min on ice. Obtained data were analyzed according to the  $K_D$  model based on the fluorophore's temperature related intensity change (TRIC) with standard settings ("cold region" from -1 to 0 s, "hot region" from 0.5 to 1.5 s) using the MO.AffinityAnalysis V2.3 software (NanoTemper Technologies). Curve fitting for data presentation was performed by GraphPad Prism 8 version 8.4.3 ('one site – total binding') based on data exported from MO.AffinityAnalysis software.

### Confocal Microscopy

BMDMs were transfected with V5-HDAC9 using electroporation. Cells were allowed to recuperate and either stimulated with LPS and nigericin or left unstimulated. Following washing with 1× PBS, cells were fixed with 4% paraformaldehyde-PBS solution for 10 minutes, and permeabilized using 0.1% Triton X. Cells were then blocked for 1 hour with 0.2% FCS, 0.2% BSA, and 0.002% fish skin gelatin in 1× PBS. Primary antibodies against NLRP3 and V5 were incubated overnight at 4°C. 4,6-diamidino-2-phenylindol as well as Cy3 and Alexa Fluor 488-labeled secondary antibodies were incubated for 1 hour at room temperature. Cells were washed and sealed with a coverslip coated in fluoromount mounting medium (Sigma). Imaging was performed with the confocal microscope (LSM 880, Zeiss) using the 40× oil objective and analyzed with the ZEN software (Zeiss).

### Multiplex cytokine profiling assay

Cytokine profiling in plasma samples was performed using ProcartaPlex™ Immunoassay Kit according to manufacturer's recommendations. Specifically, plasma generated from EDTA-buffered blood samples were incubated with high sensitivity magnetic beads for quantitative multiplex analysis. Following 2 h incubation on a plate shaker, several washes, addition of biotinylated detection antibody, and streptavidin PE, the analytes were measured with a Luminex 200 instrument with the xPONENT software. The ProcartaPlex Analysis software was used to determine the exact concentration of individual cytokines.

### Cell culture, transfection, and gene silencing

HEK293 cells were cultured in Dulbecco's modified Eagle's medium (DMEM) supplemented with 10% heat-inactivated fetal calf serum (FCS) and 1% penicillin-streptomycin–glutamine solution (Thermo Fisher Scientific). Transfection with plasmid DNA was performed with polyfectamine reagent (Qiagen) following the manufacturer's instructions. Transfection of primary macrophages (BMDMs) with pre-designed ON-TARGETplus SMARTpool mouse *Hdac9* siRNA, non-targeting control (Dharmacon), or plasmid DNA was achieved either by electroporation using mouse macrophage Nucleofector Kit (Lonza) or with Lipofectamine LTX Reagent (Invitrogen). Following electroporation, cells were allowed to recuperate for 48 h before stimulation and lysis for further analysis. Human THP-1 monocytes were cultured in RPMI medium supplemented with 10% FCS and 0.1% Gentamicin. Differentiation to macrophages was achieved by stimulation with PMA (100 nM) for 72 h.

### Generation of bone marrow-derived macrophages

Bone marrow-derived macrophages (BMDMs) were generated as established by flushing the bone marrow from femurs and tibiae with ice-cold PBS, resuspending in PBS by repeated pipetting and filtering through a 40  $\mu\text{m}$  cell strainer (BD Biosciences). After centrifugation of the cell suspension at 500 g for 10 min, the pellet was resuspended in culture medium (RPMI 1640 containing 10% FCS, 15% L929-cell-conditioned medium (LCM) and 50 mg/mL gentamycin) and plated on 15 cm untreated culture plates (Greiner). 15 % fresh L929-conditioned medium (LCM) was added again on day 2 and 3 of culturing. For stimulation experiments, differentiated macrophages were harvested by gentle scraping, transferred into untreated 6-well or 12-well plates (Greiner) on

Day 7 of culturing and left in LCM-free medium for 24 hours, allowing cells to adhere. Cells were then stimulated in FCS-free medium with specific stimulus at different time intervals or left untreated.

### Inflammasome activation assay

Following generation of BMDMs, cells were seeded in 6-well plates and were either primed with 300 ng/mL LPS (*Escherichia coli* O111:B4) for 3 hours before replacing with serum-free medium containing nigericin at the concentration of 5 mM for 45 min or 100 ng/mL for 4 hours followed by nigericin stimulation for 1 hour. Cell lysates and corresponding supernatant were harvested for further analysis. For rapid priming experiments in Figures S6A–S6H, cells were co-stimulated with LPS and nigericin to simultaneously engage TLRs and NLRP3. Specifically, BMDMs were treated with TMP195 (5  $\mu$ M) for 1 hour and thereafter were simultaneously stimulated with LPS (200 ng/mL) and nigericin (5  $\mu$ M) for 1 hour before cell lysis and further analyses.

### Blue native gel electrophoresis for NLRP3 oligomerization

Blue native gel electrophoresis was performed using the Bis-Tris Native PAGE system as established and previously described.<sup>27,72,73</sup>  $3 \times 10^6$  HEK293 cells were plated in 60 mm dishes and transfected with 2  $\mu$ g each of the indicated plasmids. Following transfections, the cells were stimulated with 5  $\mu$ M nigericin for 1 hour, washed once with cold PBS and lysed in ice-cold native lysis buffer (20 mM Bis-tris, 500mM  $\epsilon$ -aminocaproic acid, 20 mM NaCl, 10% (w/v) glycerol, 0.5% digitonin, 0.5 mM  $\text{Na}_3\text{VO}_4$ , 1mM PMSF, 0.5mM NaF, 1 $\times$  EDTA-free Roche protease inhibitor cocktail and Roche PhosSTOP inhibitor, pH 7.0) for 15 min on ice. Cell lysates were clarified by centrifugation at 18,000g for 30 min at 4 $^\circ$ C and analysed without further purification steps. Total proteins were quantified using the Pierce BCA protein assay (#23225, ThermoFisher). Samples were separated on 3-12% blue native PAGE (#BN1001BOX, Invitrogen). Native gels were incubated in 10% SDS solution for 5 min before transfer to PVDF membranes (Millipore), followed by conventional western blotting.

### ASC oligomerization

ASC oligomerization was performed as previously described by Lugrin and Martinon<sup>74</sup> and established in our laboratory.<sup>75</sup> In detail, bone marrow cells were isolated from mice and differentiated with L929-cell-conditioned medium. For priming of the inflammasome, cells were washed with PBS and stimulated with 100 ng/ml of LPS for 3 h. Activation of the inflammasome was achieved by stimulation with 5  $\mu$ M nigericin for 60 min. Cells were washed in PBS containing 2 mM EDTA and detached by scraping. After centrifugation, cell pellets were resuspended in 0.5 ml of ice-cold Buffer A (20 mM HEPES-KOH, pH 7.5, 10 mM KCl, 1.5 mM  $\text{MgCl}_2$ , 1 mM EDTA, 1 mM EGTA, 320 mM sucrose) and lysed through sonification. After centrifugation to remove bulk nuclei, 20  $\mu$ l of lysate was stored as input prior to oligomerization. Buffer A was added to the remaining lysate and following centrifugation, supernatants were diluted with CHAPS buffer (20 mM HEPES-KOH, pH 7.5, 5 mM  $\text{MgCl}_2$ , 0.5 mM EGTA, 0.1 mM PMSF, 0.1% CHAPS) and pelleted through centrifugation. Proteins were cross-linked for 30 min at room temperature with 50  $\mu$ l of CHAPS Buffer containing 4 mM of DSS (Disuccinimidyl suberate). After centrifugation pellets were resuspended in 1x lithium dodecyl sulfate (LDS) buffer and boiled at 70  $^\circ$ C for 10 min. Samples were loaded onto SDS-PAGE and separated at 150 V. Transfer was performed at 4  $^\circ$ C and 100 V for 1 h and membranes blocked with 5% BSA in TBST. Membranes were incubated overnight at 4  $^\circ$ C with Anti-ASC antibody (Adipogen, AL177), washed three times in TBST and incubated at room temperature for 1 h with Goat Anti-Rb HRP antibody. After washing and detecting the images, membranes were re-incubated with Actin-antibody for 1 h at room temperature followed by washing and incubation with secondary antibody. Protein bands were visualized with a Fusion Fx7.

### HDAC9 activity assay

Fluorogenic HDAC9 assay kit was purchased from BPS Bioscience and HDAC9 activity performed according to the manufacturer's instructions. Briefly, a master mix consisting of fluorogenic acetylated peptide substrate for class IIa (200 $\mu$ M), BSA (1mg/ml) and HDAC assay buffer was prepared and added to a low binding 96-well microtiter plate. HDAC9 human recombinant enzyme (0.6 ng/ $\mu$ l) was added to all wells except for wells designated as blank. Trichostatin A (100  $\mu$ M) served as a control to assess the inhibitory activity and cell lysis buffer alone was used as the background solution for both blank and positive control. Following incubation of the plate at 37 $^\circ$ C for 30 min, undiluted HDAC assay developer (2x) was added at room temperature for 15 min. The fluorescence intensity was measured using GloMax<sup>®</sup>-Multi Detection System at excitation wavelength of 365 nm and emission wavelength of 410-460 nm. All samples were measured in duplicates and the blank subtracted from resulting values.

### ELISA

For maturation and release of IL-1 $\beta$  and IL-18, BMDMs were stimulated with LPS and nigericin. Levels of IL-1 $\beta$  and IL-18 were measured in supernatants using commercially available ELISA kits (R&D systems). Likewise, the secretion of human IL-1 $\beta$  and IL-18 were quantified using commercially available ELISA kits (Invitrogen and R&D systems).

### Detection of lytic cell death

To determine NLRP3/GSDMD-induced lytic cell death, we used two independent methods: LDH release and Zombie uptake. LDH release was determined in supernatants of BMDMs stimulated with LPS and nigericin. The assay was performed using the Pierce LDH cytotoxicity assay kit following manufacturer's instructions (Thermo Fisher Scientific). LDH release was calculated as LDH release [%] = (LDH activity in stimulated cells – spontaneous LDH activity in unstimulated cells) / (Maximum LDH activity after

complete lysis – spontaneous LDH activity)  $\times$  100. Uptake of Zombie dye, a second independent methodology to assay membrane integrity, was assessed in BMDMs stimulated with LPS and nigericin following manufacturer's instructions (Biolegend). Cells were washed with  $1\times$  PBS and fixed with 4% paraformaldehyde-PBS solution for 10 minutes. Nuclei was counterstained with 4,6-diamidino-2-phenylindol and images acquired with  $20\times$  objective.

### Flow cytometry

Aorta and EDTA-buffered blood samples were harvested, and a single-cell suspension was prepared and filtered over a  $70\ \mu\text{m}$  cell strainer (Greiner). Cells were treated with erythrocyte lysis buffer ( $0.155\ \text{M}\ \text{NH}_4\text{Cl}$ ,  $10\ \text{mM}\ \text{NaHCO}_3$ ). All cell suspensions were carefully washed and stained with FACS staining buffer and combinations of antibodies against Cd45, Cd11b, Cd3, B220, Ly6G (eBioscience), and Ly6C (Miltenyi Biotec). Flow cytometry analysis was performed using FACSVerse and FACSuite software (BD Biosciences) after appropriate fluorescence compensation, and leukocyte subsets were gated using FlowJo software (TreeStar). B cells were identified as  $\text{Cd}45^+\text{B}220^+$ ; T cells as  $\text{Cd}45^+\text{Cd}3^+$ ; neutrophils as  $\text{Cd}45^+\text{CD}11\text{b}^+\text{Ly}6\text{G}^+$ ; monocytes as  $\text{Cd}45^+\text{Cd}11\text{b}^+\text{Ly}6\text{C}^+$ .

### Transcriptomic profiling

BMDMs were isolated from *Hdac9<sup>ΔCRE</sup>ApoE<sup>-/-</sup>*, *Hdac9<sup>-/-</sup>ApoE<sup>-/-</sup>*, and *ApoE<sup>-/-</sup>* mice as established and briefly described above. Cells were stimulation with LPS ( $100\ \text{ng/mL}$ ) for 6 hours in serum-free condition. Cells were preserved in RLT buffer with  $\beta$ -mercaptoethanol and total RNA was later isolated with the Maxwell RSC48 instrument and miRNA Tissue Kit (Promega, Fitchburg, USA). The RNA concentration was determined using a Nanodrop spectrometer (Thermo Fisher Scientific, Waltham, MA, USA), and RNA quality was assessed using an Agilent Bioanalyzer (Agilent RNA 6000 Nano kit, Agilent Technologies, Santa Clara, CA, USA). Libraries were prepared using the Lexogen CORALL mRNA-seq Library Prep Kit V2 (Lexogen, Vienna, Austria) at half the volume recommended in the manual. In summary,  $200\ \text{ng}$  of total RNA were captured on oligo-dT beads and reverse transcribed directly on the beads, followed by the synthesis of the second cDNA strand after adapter ligation. The adapted cDNA was eluted and then amplified with bar-coded primer. The finalized, barcoded libraries were pooled and sequenced on an Illumina NextSeq 2000 (Illumina, San Diego, CA, USA) with a read length of 60 nucleotides in paired-end mode. For sequence analysis of RNA reads, 50-nt single-end reads were mapped to the GRCm38 reference genome using STAR software, version 2.6.1d. TPM expression values based on ENSEMBL annotation, version GRCm38.95, were calculated with RSEM (1.3.0). We used the DESeq2 Bioconductor R package to identify differentially expressed genes at a false discovery rate of 10% as shown in Figure S6I. Pathway analyses were generated through the use of QIAGEN IPA (QIAGEN Inc., <https://digitalinsights.qiagen.com/IPA>) as shown in Figures S6J–S6M. Transcriptomics data is available online under the accession number GSE274312.

### Quantitative real-time PCR

RNA was isolated using the RNeasy Mini Kit (Qiagen) and reverse-transcribed using oligodT primers (Metabion). RT-PCR analysis was performed using Brilliant II SYBR Green QPCR Master Mix (Agilent Technologies) or Taqman probes in a Light cycler 480 (Roche Diagnostics). *GAPDH*, *HPRT1* or  $\beta$ -*Actin* were used as housekeeping genes for normalization, as appropriate. For HDAC9 detection, two Taqman probes were selected to detect the expression of short isoform MITR and long isoform HDAC9. Measurements were performed in triplicates. The  $2^{-\Delta\Delta\text{Ct}}$  method was used to calculate relative expression changes. Primers are listed in Table S3.

### Magnetic activated cell sorting (MACS)

Single-cell suspension was prepared and filtered over MACS pre-separation filter (Miltenyi). Thereafter, cells were treated with erythrocyte lysis buffer ( $0.155\ \text{M}\ \text{NH}_4\text{Cl}$ ,  $10\ \text{mM}\ \text{NaHCO}_3$ ) and cell suspensions carefully washed, re-suspended in MACS running buffer, and total cell number determined. MACS antibodies were added according to kit-specific instructions. After incubation at  $4^\circ\text{C}$  for 30 minutes (incubation time vary depending on the specific kit), cell suspension was washed 2 times with MACS running buffer at  $4^\circ\text{C}$  at  $500\times g$  for 5 min. Cell pellet was re-suspended in  $500\ \mu\text{l}$  MACS running buffer and sorted by Auto MACS machine. Kit specific selection program was chosen. After sorting, cells were pelleted by centrifugation and washed 2 times with PBS. Thereafter, cell pellets were directly lysed in QIAzol reagent and immediately snap frozen for later RNA isolation.

### Statistical tests

Statistical analyses were performed with GraphPad Prism 9. Results are reported as means  $\pm$  s.e.m. After testing for normality with Shapiro-Wilk-Test and visual inspection of the QQ plots, data were analyzed by two-tailed unpaired Student's t test for a two-group normally distributed datasets or Mann-Whitney test for non-normally distributed data. For multiple comparisons, one-way or two-way ANOVA with Bonferroni or Holm-Sidak test or two-stage set-up method of Benjamini, Krieger, and Yekutieli multiple comparisons test or Kruskal-Wallis with Dunn's test were used as appropriate. P values  $<0.05$  were considered to be statistically significant.